Lithos 390–391 (2021) 106097

Contents lists available at ScienceDirect

Lithos

journal homepage: www.elsevier.com/locate/lithos

Research Article

Reworking of juvenile crust beneath the Bangong–Nujiang suture zone: Evidence from Late Cretaceous granite porphyries in Southern Qiangtang, Central Tibet

Zi-Long Wang [a,b,c], Jing-Jing Fan [a,b,c], Qiang Wang [a,b,c,*], Wan-Long Hu [a,c], Zong-Yong Yang [d], Jun Wang [a,c]

[a] State Key Laboratory of Isotope Geochemistry, Guangzhou Institute of Geochemistry, Chinese Academy of Sciences, Guangzhou 510640, China
[b] College of Earth and Planetary Sciences, University of Chinese Academy of Sciences, Beijing 100049, China
[c] CAS Center for Excellence in Deep Earth Science, Guangzhou 510640, China
[d] State Key Laboratory of Ore Deposit Geochemistry, Institute of Geochemistry, Chinese Academy of Sciences, Guiyang 550002, China

ARTICLE INFO

Article history:
Received 23 November 2020
Received in revised form 2 March 2021
Accepted 2 March 2021
Available online 8 March 2021

Keywords:
Granite porphyry
Later stage of Late Cretaceous
Juvenile crustal reworking
Post-collision extension
Central Tibet

ABSTRACT

Crustal reworking in the collisional zones is commonly considered as an important process to result in continental crust differentiation and maturation. However, the reworking mechanism remains unclear. Here, a combined study of zircon SIMS U–Pb age, whole-rock major and trace element, Sr–Nd–Hf and zircon Hf–O isotopic geochemistry was carried out for the Duoma–Namuqie (DM–NMQ) granite porphyry intrusions, including DM, NMQ I, II and III intrusions, in southern Qiangtang, central Tibet. Zircon SIMS U–Pb dating yielded ages of 79–76 Ma, suggesting that they were formed in the later stage of Late Cretaceous. The DM granite porphyries are metaluminous to peraluminous with slightly low SiO_2 (69.2–71.4 wt%) and high MgO (0.67–0.79 wt%) contents. They are depleted in high-field-strength elements (HFSEs) and enriched in light rare earth elements (LREEs), large ion lithophile elements (LILEs), and show weakly negative Eu anomalies. The NMQ III granite porphyries show similar elemental features to the DM granite porphyries, but have relatively high SiO_2 (69.8–72.2 wt%) and low MgO (0.25–0.28 wt%) contents. Both of them belong to I-type granites. The NMQ I and II granite porphyries are relatively differentiated with high SiO_2 (76.4–77.9 wt%), low MgO (0.11–0.16 wt%) contents, and significantly negative Eu anomalies. Extremely low LREE contents and notable REE tetrad effect can be observed in the NMQ II granite porphyries. The NMQ I and II intrusions are fractionated I-type granites. The whole-rock Sr–Nd–Hf and zircon Hf–O isotope data exhibit an enriched trend from the DM granite porphyries ($(^{87}Sr/^{86}Sr)_i$ = 0.7049–0.7050, $\varepsilon_{Nd}(t)$ = 1.2–1.6, $\varepsilon_{Hf}(t)_{whole\text{-}rock}$ = 9.9–12.0, $\varepsilon_{Hf}(t)_{zircon}$ = 7.4–11.5, $\delta^{18}O$ = 6.2–7.1‰) to the NMQ III granite porphyry ($(^{87}Sr/^{86}Sr)_i$ = 0.7058–0.7067, $\varepsilon_{Nd}(t)$ = −0.9 to −1.1, $\varepsilon_{Hf}(t)_{whole\text{-}rock}$ = 7.0–7.4, $\varepsilon_{Hf}(t)_{zircon}$ = 2.7–9.5, $\delta^{18}O$ = 7.2–7.6‰) to the NMQ I and II granite porphyries ($\varepsilon_{Nd}(t)$ = −3.0 to −4.3, $\varepsilon_{Hf}(t)_{whole\text{-}rock}$ = 5.3–6.6, $\varepsilon_{Hf}(t)_{zircon}$ = 1.5–7.4, $\delta^{18}O$ = 6.6–9.2‰). We suggest that the DM–NMQ granite porphyries were mainly derived by partial melting of the juvenile mafic lower crust with variable volumes of ancient crustal components involved in their magma sources. The way in which these granite porphyries were formed provides evidence for the crustal differentiation and maturation in a post-collisional extensional setting triggered by the far-field rollback of the subducted Neo-Tethys oceanic slab

1. Introduction

The growth of continental crust is an important scientific research topic that continues to stimulate intense debate. It is widely accepted that continental crustal growth occurs primarily in subduction zones, either by vertical addition of underplated basaltic magmas at the crust–mantle interface, or by lateral accretion of island or intra-oceanic arc complexes and oceanic plateaus, as revealed by the arc-like element signature of the bulk continental crust (Chen and Arakawa, 2005; Niu et al., 2013; Rudnick and Gao, 2003). However, numerous studies have proposed that continental collision zones are ideal sites for crustal growth, and this hypothesis has been verified in several orogenic belts, including the east Kunlun, Gangdese, and western Qinling belts (e.g., Niu et al., 2013). The key to this apparent contradiction involves distinguishing growth from reworking of juvenile crust at convergent plate boundaries. Given that juvenile continental crust formed at arc settings is too mafic for their composition, an additional process is thus required to transform the juvenile basaltic crust into mature continental crust (Tang et al., 2019a). Two main mechanisms have been proposed for this transformation. One is partial melting of the underplated

* Corresponding author at: State Key Laboratory of Isotope Geochemistry, Guangzhou Institute of Geochemistry, Chinese Academy of Sciences, Guangzhou 510640, China.
E-mail address: wqiang@gig.ac.cn (Q. Wang).

https://doi.org/10.1016/j.lithos.2021.106097
0024-4937/

basaltic rocks, either in a subduction zone or a collision zone (Hao et al., 2016; Tang et al., 2019b). The second is weathering of juvenile crust, followed by burial and melting of juvenile crust sediments in a collision zone (Tang et al., 2019a; Wu et al., 2006).

Granitoids and their volcanic equivalents are the most abundant constituent of continental crust, and knowledge of their origin is essential for understanding the evolution and differentiation of the continental crust. The Bangong–Nujiang suture zone (BNSZ) on the Tibetan Plateau records the evolution of Meso-Tethys oceans from the Early–Middle Jurassic to the Early Cretaceous (Wang et al., 2016; Zhu et al., 2016). Widespread granitoid batholiths from three episodes of magmatism, namely, the Jurassic (170–150 Ma), Early Cretaceous to the early stage of Late Cretaceous (126–95 Ma), and the later stage of Late Cretaceous (80–68 Ma), have been found along the BNSZ. Batholiths of the first two episodes were formed as a result of subduction and closure of the Bangong–Nujiang Tethys Ocean (BNTO; i.e., volcanic-arc and syn-collisional settings), whereas batholiths of the third episode were formed in a post-collisional or intra-continental setting (Chen et al., 2017; He et al., 2019; Hu et al., 2019; Li et al., 2013; Zhao et al., 2008; Zhu et al., 2016).

Here we focus on the Late Cretaceous magmatic episode. Widespread Late Cretaceous magmatic rocks (100–70 Ma) with positive $\varepsilon_{Nd}(t)$ and $\varepsilon_{Hf}(t)$ values have been recognized in the Lhasa terrane (Fig. 1a). They were formed in an arc setting related to the subduction of Yarlung–Zangbo oceanic lithosphere (Ma et al., 2013a, 2013b; Tang et al., 2019b). The early-stage magmatism (100–85 Ma) is dominated by mantle-derived mafic intrusions, indicating substantial crustal growth (Ma et al., 2013a, 2013b). Most of the late-stage magmatism (85–70 Ma) are felsic, and are considered products of juvenile crust reworking by partial melting of pre-existing underplated basaltic lower crust (Tang et al., 2019b). However, the Qiangtang terrane in the Late Cretaceous was in a post-collisional or intra-continental setting, and whether crustal growth or reworking occurred remains unclear.

In this study, we present a combined study of zircon U–Pb dating and Hf–O isotopes, and whole-rock elements and Sr–Nd–Hf isotopes for the Late Cretaceous Duoma–Namuqie (DM–NMQ) granite porphyries in the southern Qiangtang subterrane (SQT), adjacent to the BNSZ. The goals of this study are to systematically investigate their petrogenesis and establish the mode of juvenile crust reworking and its contribution to continental maturation in a post-collisional setting.

2. Geological setting and samples

The Tibetan Plateau consists of four terranes or blocks, namely, the Songpan–Ganzi, Qiangtang, Lhasa, and Himalaya terranes/blocks, from north to south. They are separated by the Jinsha, Bangong–Nujiang, and Indus–Yarlung–Zangbo suture zones (Fig. 1a), respectively, which represent Paleo-, Meso-, and Neo-Tethyan oceanic relicts, respectively.

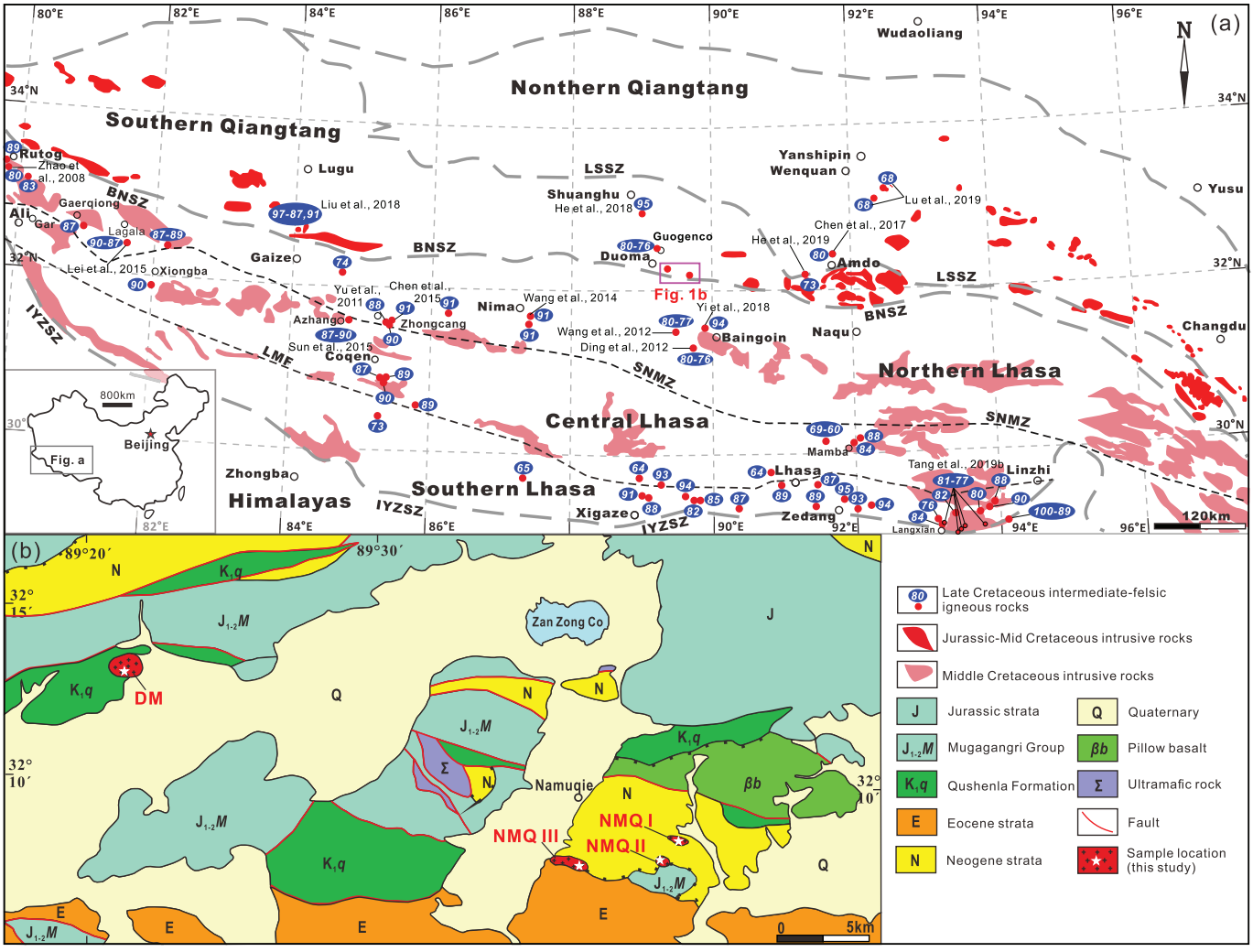

Fig. 1. (a) Tectonic units of the Tibet showing the major subdivisions and distributions of Late Mesozoic intrusive rocks (Zhang et al., 2012). Literature data for the Late Cretaceous intermediate-felsic igneous rocks are listed in Table S6. (b) Simplified regional geological map of the Duoma–Namuqie area, Southern Qiangtang Terrane.

The Qiangtang terrane is divided into northern and southern Qiangtang subterranes by the Shuanghu–Longmucuo suture zone (Li et al., 2006), which is characterized by Mesozoic HP–UHP metamorphic rocks, Paleozoic ophiolites, and subduction- or collision-related magmatism (Zhang et al., 2012). The SQT is covered by Triassic–Late Jurassic terrestrial deposits, including Carboniferous and Permian interbedded sandstone and shale, Late Triassic limestone, and Middle–Late Jurassic clastic rocks and carbonates. The Late Triassic–Late Jurassic marine deposits are unconformably overlain by weakly deformed Late Cretaceous continental sediments (i.e., the Abushan Formation) that were the products of collision between the Qiangtang and Lhasa terranes (Kapp et al., 2007; Li et al., 2013; Zhang et al., 2012). Numerous late Mesozoic intermediate–felsic magmatic rocks (183–73 Ma; Chen et al., 2017; Hao et al., 2019; He et al., 2019; Li et al., 2013; Liu et al., 2014a; Zhang et al., 2012) are widely distributed in the SQT from the Rotug to Changdu areas (Fig. 1a).

The BNSZ, extending over 2000 km in central Tibet, represents remnants of the BNTO and is mainly composed of Jurassic–Cretaceous flysch, mélange, and scattered ophiolitic fragments (Fig. 1a; Leier et al., 2007; Schneider et al., 2003). Two major magmatic belts, i.e., the Jurassic (185–150 Ma) and Early Cretaceous (126–100 Ma) magmatic belts, have been identified in the SQT along the BNSZ (Fig. 1a), which may record the processes related to slab subduction and closure of the BNTO, respectively (He et al., 2018; Zhang et al., 2012; Zhu et al., 2016). In addition, their spatiotemporal distributions may indicate diachronous closure of the BNTO (Hu et al., 2019), i.e., closure of the eastern part during the later stage of Early Cretaceous (Kapp et al., 2007; Zhu et al., 2016), and closure of the western and western-central parts in the Late Cretaceous (Hao et al., 2019; Zhang et al., 2012, 2014).

The Lhasa terrane is divided into northern, central, and southern subterranes by the Shiquanhe–Nam Tso Mélange Zone (SNMZ) and Luobadui–Milashan Fault (LMF), respectively (Fig. 1a) (Zhu et al., 2013). The central Lhasa subterrane has an Archean–Proterozoic crystalline basement, whereas the southern and northern Lhasa subterranes are characterized by the occurrence of juvenile crust. The northern Lhasa subterrane (NLS) is dominated by Middle Triassic to Cretaceous sedimentary rocks, in which the Late Cretaceous Jingzhushan Formation molasse unconformably overlies the older strata (Zhu et al., 2013). Abundant Cretaceous magmatic rocks are widely exposed in the NLS (Fig. 1a).

The DM–NMQ area is on the southern margin of the SQT adjacent to the BNSZ (Fig. 1b). The main lithostratigraphic units in this area include the Early Cretaceous Qushenla Formation volcanic rocks (e.g., andesite, tuff sandstone, and crystal tuff), and Early–Middle Jurassic Mugagangri Group accretionary complex (e.g., metasandstone, siliceous rocks, and minor ophiolitic mélange), which record the accretion process of the northward subduction of Meso-Tethys oceanic lithosphere. The later stage of Early Cretaceous OIB-type basalts in this area have geochemical characteristics similar to those of the Hawaiian basalts (Zhu et al., 2006, 2016), and are considered to be part of the oceanic plateau of the BNTO (Zhang et al., 2014).

Granite porphyries were selected from four small plutons (DM and NMQ I, II, and III). The samples are porphyritic, with phenocrysts of plagioclase (0.5–1 mm), biotite (0.5–1 mm), and quartz (0.1–0.3 mm; Fig. 2a–d). In addition, some euhedral amphibole crystals (0.5–1 mm) can be observed in the DM granite porphyries (Fig. 2a). The groundmass of these granite porphyries consists primarily of microlitic quartz and plagioclase.

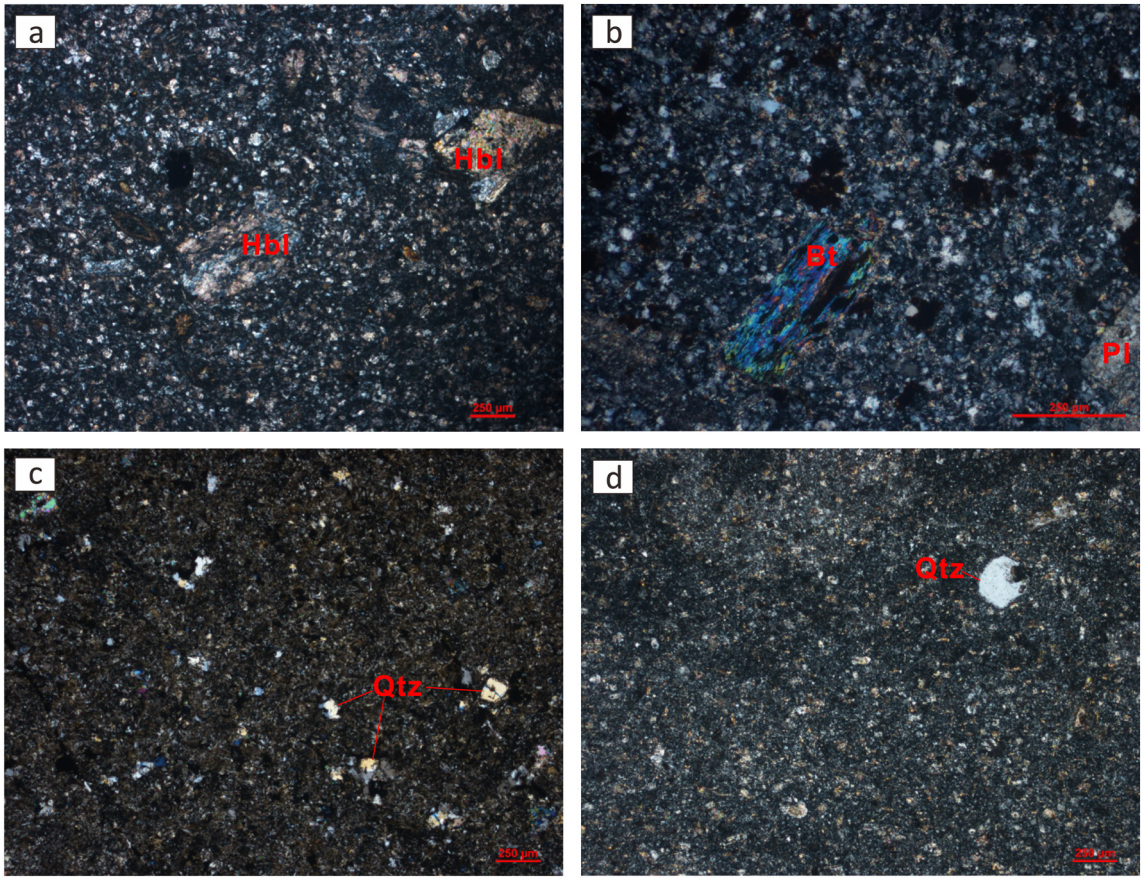

Fig. 2. Representative photomicrographs (cross-polarized light) of the Duoma–Namuqie granite porphyries: (a) Duoma hornblende-bearing granite porphyries and (b)–(d) NMQ III, NMQ I and NMQ II granite porphyries. Mineral abbreviations: Bt–biotite; Hbl–hornblende; Pl–plagioclase; Qtz–quartz.

3. Analytical methods

Samples for geochemical analyses first had their surfaces removed with a diamond saw, with the remaining fresh sample broken into small chips and cleaned using 2% HCl and distilled water. Samples were then dried and powdered to ~200 mesh using an agate mortar. All analyses were conducted at the State Key Laboratory of Isotope Geochemistry, Guangzhou Institute of Geochemistry, Chinese Academy of Sciences, Guangzhou, China. Analytical methods, including whole-rock geochemical analyses, and zircon U–Pb dating and Hf–O isotope analyses for the DM–NMQ granite porphyry samples are given in Supplementary File S1.

4. Results

4.1. Zircon U–Pb geochronology

Zircon U–Pb age data are presented in Supplementary Table S1. Zircon crystals from the DM sample (16DM17-1) are narrow with aspect ratios of 1.5–5, which indicates a rapid crystallization process typical of porphyritic, sub-volcanic intrusions, and high-level granites. Most of the zircons have well-developed oscillatory zoning that is characteristic of magmatic zircon (Fig. 3a). They have Th/U ratios of 0.43–0.94. Eighteen analyses of these zircon grains yielded a concordant $^{206}Pb/^{238}U$ age of 76.0 ± 0.6 Ma (MSWD = 0.23, 2σ; Fig. 3b).

Zircon grains separated from the NMQ III granite porphyry (NMQ04-9) are mostly translucent and euhedral and show well-developed oscillatory zoning (Fig. 3a). The zircon grains vary in size from 50 μm × 150 μm to 100 μm × 300 μm and have aspect ratios of 1.5–3. They have Th/U ratios of 0.33–1.43. Sixteen analyses of these zircon grains yielded a concordant $^{206}Pb/^{238}U$ age of 78.2 ± 0.6 Ma (MSWD = 0.04, 2σ; Fig. 3c).

Zircon grains separated from the NMQ I granite porphyry (NMQ01-5) are mostly euhedral with aspect ratios of 1.5–3. Most of the grains have oscillatory zoning typical of magmatic zircon in granitic rocks. Twenty-two spot analyses were conducted on 21 zircon grains, with eight grains with Th/U ratios of 0.67–2.87 yielding a concordant $^{206}Pb/^{238}U$ age of 78.9 ± 0.9 Ma (MSWD = 0.01, 2σ; Fig. 3d). Age data for the other 13 grains were disregarded on account of the dark color and high U and Th contents of these grains.

Zircon grains from the NMQ II granite porphyry (NMQ03-7) are mostly dark, possess cracks, and show no oscillatory zoning. We disregarded age data for these zircon grains owing to their extremely high U and Th contents. Considering that i) the zircons from NMQ II granite porphyry exhibit similar crystal shapes to the dark zircons in sample NMQ I porphyry (Fig. 3), and ii) NMQ I and II granite porphyry plutons occur in the same area (Fig. 1), and their porphyries have

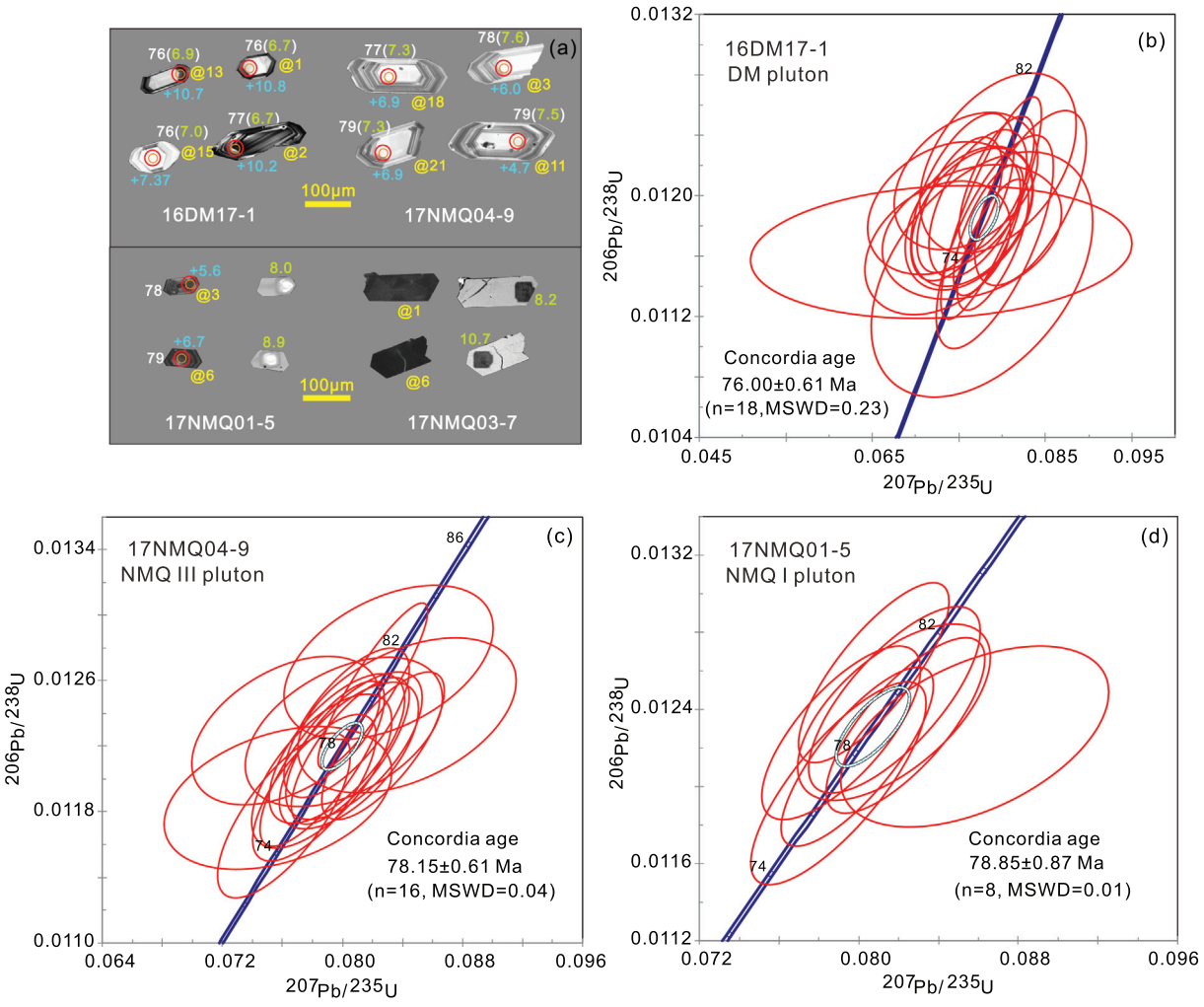

Fig. 3. Cathodoluminescence (CL) and BSE images of zircons (a) and SIMS zircon U—Pb ages for Duoma–Namuqie granite porphyries (c–d). Zircon internal textures and surface features are revealed and spot locations of zircon isotopic analyses are marked. The blue number represents the Hf isotope value (red circle) and the orange number represents the O isotope value (orange-red circle). The white numbers near the analysis spots in CL images are the U—Pb dates (Ma). The yellow scale bars in CL images are 100 μm long.

similar field (Fig. S1) and petrographical (Fig. 2c, d) observations and some element (e.g., HREEs, Ba, Nb, Ta, Ti, Zr and Sm) characteristics, we speculate that the NMQ II porphyry may have an identical formation age to that of the NMQ I intrusion.

4.2. Alteration effects

Whole-rock major- and trace-element data are listed in Supplementary Table S2. Samples from the DM and NMQ intrusions have variable loss-on-ignition (LOI) values with lower values of 0.90–2.12 for the NMQ I and II granite porphyries, and slightly higher values of 2.12–3.54 for the NMQ III and DM granite porphyries. Thus, the effects of alteration must be carefully evaluated. Generally, HFSEs, REEs, Th, and transition elements (e.g., Fe, Mn, and Ti) are essentially immobile during hydrothermal alteration (Hawkesworth et al., 1997), whereas LILEs, (e.g., Ca, Na, K, Sr, Ba, and Rb) are generally mobile. The lack of correlations between LOI and K_2O, Na_2O, Al_2O_3, MgO, $Fe_2O_3^T$, and P_2O_5 (Fig. S2a–b, d–g) indicates negligible alteration effects on these elements. However, in the LOI vs. CaO diagram, for the NMQ II samples with LOI contents <1.6 wt% and the NMQ III samples with LOI contents <2.6 wt%, CaO contents are relatively constant, but for samples (NMQ03-–2, NMQ03-5, NMQ04-5, and NMQ04-9) with LOI contents higher than these two respective values, CaO contents markedly increase (Fig. S2c), indicating the effect of hydrothermal alteration. In addition, Rb contents and $(^{87}Sr/^{86}Sr)_i$ ratios of the NMQ I and II samples show positive correlations with LOI (Fig. S2h–i), also suggesting a possible influence of alteration (Wang et al., 2006a). Thus, CaO contents of the four samples NMQ03-2, NMQ03-5, NMQ04-5, and NMQ04-9 from the NMQ II and III intrusions and the Rb–Sr systematics of the NMQ I and II granite porphyries are not discussed below.

4.3. Major- and trace-element geochemistry

The DM granite porphyries have relatively homogeneous and high SiO_2 (69.2–71.4 wt%), MgO (0.67–0.79 wt%), $Fe_2O_3^T$ (1.70–2.17 wt%), K_2O (2.86–3.14 wt%), Na_2O (3.33–3.92 wt%), and CaO (1.86–2.88 wt%) contents and $Mg^{\#}$ (39–47) values, and moderate Al_2O_3 (14.4–14.7 wt%) values. In the (K_2O + Na_2O) vs. SiO_2 diagram, most of the samples fall within the granite field, except one sample (16DM17–2) that plots within the granodiorite field (Fig. 4a). In the (Na_2O + K_2O – CaO) vs. SiO_2 binary diagram, these samples drop in the calc-alkaline and calcic area (Fig. 5a). Values of the A/CNK ratio (molecular ratio of $Al_2O_3/(CaO + Na_2O + K_2O)$) (1.04–1.14) and $FeO^t/(FeO^t + MgO)$ (0.53–0.61) indicate that the DM samples are metaluminous to peraluminous and magnesian (Figs. 4b and 5b). Granite porphyries from the NMQ III pluton have similar SiO_2 (69.8–72.2 wt%), $Fe_2O_3^T$ (1.96–2.30 wt%), K_2O (2.66–3.47 wt%), and Na_2O (3.31–3.98 wt%) contents but lower MgO (0.25–0.28 wt%) and CaO (0.78–2.08 wt%) and higher Al_2O_3 (15.0–15.3 wt%) contents compared with the DM granite porphyries (Table S2). Most of the NMQ III granite porphyries fall within the field of granite and the peraluminous rock series (Fig. 4a–b). Chondrite-normalized REE patterns show that samples from both the DM and NMQ plutons are enriched in LREEs with $(La/Yb)_N$ ratios of 22–24 and 37–47, and have negative Eu anomalies (Eu/Eu*) of 0.70–0.79 and 0.80–0.84, respectively (Fig. 6a). The primitive mantle-normalized trace-element profiles of these samples are remarkably similar, and both exhibit negative Ba, Sr, P, Nb, Ta, and Ti anomalies and positive Rb, Th, U, and K anomalies (Fig. 6b).

The NMQ I and II granite porphyries, relative to the DM and NMQ III granite porphyries, have higher SiO_2 (76.4–77.9 wt%) and lower MgO (0.11–0.16 wt%), $Fe_2O_3^T$ (0.44–0.73 wt%), Al_2O_3 (13.4–13.8 wt%), P_2O_5 (0.01–0.02 wt%), and TiO_2 (0.05–0.06 wt%) contents. Both of them are belong to high-SiO_2, peraluminous granites (Fig. 4a–b). The NMQ I granite porphyries show similar Na_2O (3.63–3.86 wt%) but higher K_2O (3.88–4.30 wt%) contents relative to the NMQ II granite porphyries (3.86–4.80 wt% and 1.47–1.98 wt%, respectively; Table S2). Chondrite-normalized REE patterns show slight LREE enrichment for the NMQ I pluton and a pronounced tetrad effect for the NMQ II pluton (Fig. 6a). Samples of both plutons have low Eu/Eu* ratios of 0.25–0.30 and show

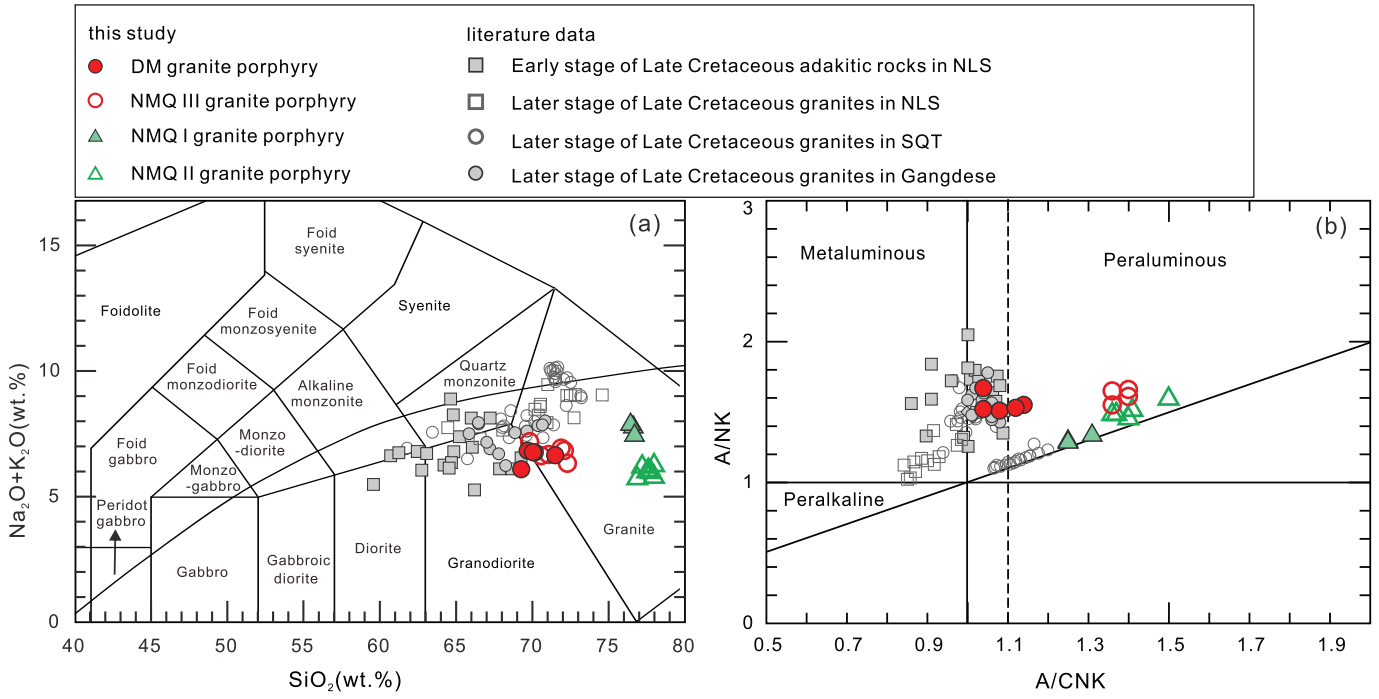

Fig. 4. Na_2O + K_2O vs. SiO_2 (a) and A/NK vs. A/CNK (b) for the DM-NMQ granite porphyries. The early stage of Late Cretaceous intermediate-felsic rocks in NLS (Lei et al., 2015; Yi et al., 2018; Yu et al., 2011), and the later stage of Late Cretaceous granites in the SQT (He et al., 2019), NLS (Ding et al., 2012; Zhao et al., 2008) and Gangdese (Tang et al., 2019b) are also plotted for comparison.

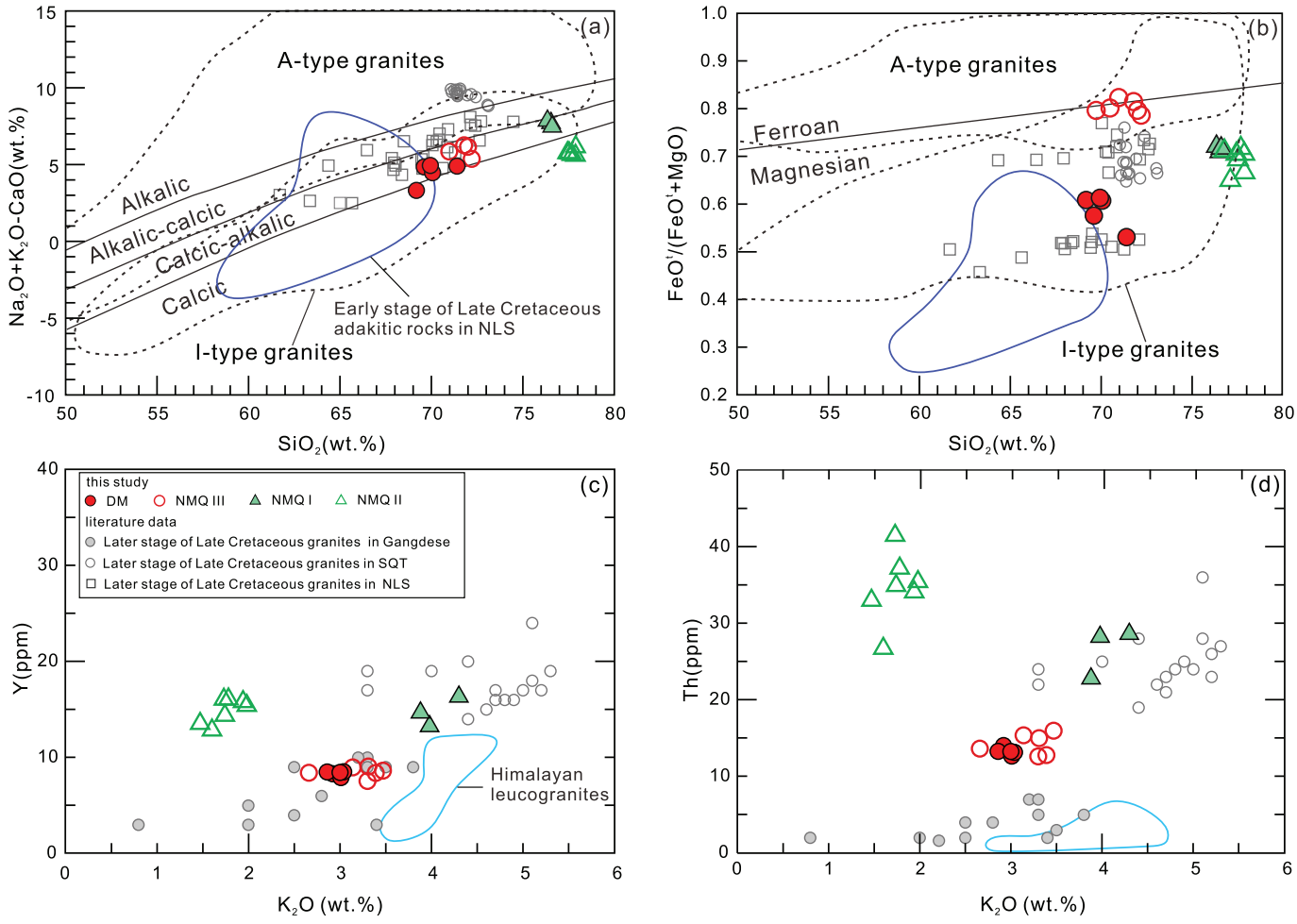

Fig. 5. $Na_2O + K_2O - CaO$ vs. SiO_2 (a), $FeO^t/(FeO^t + MgO)$ vs. SiO_2 (b), K_2O vs. Y (c) and Th (d). The approximate ranges for alkalic, alkalic-calcic, calcic-alkalic and calcic rock series and I- and A-type granites are from the compilations of Frost et al. (2001). The literature data are the same to Fig. 4.

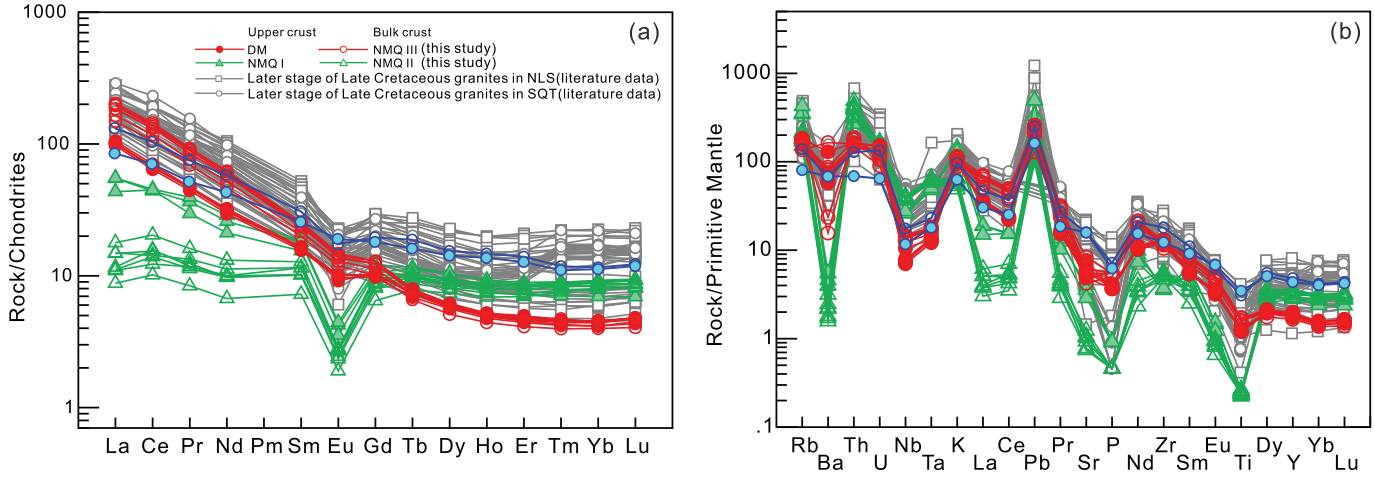

Fig. 6. Chondrite-normalized REE patterns (a) and primitive mantle normalized multi-element diagrams (b) for Duoma–Namuqie granite porphyries. The average upper continental crust and bulk continental crust compositions are from Rudnick and Gao (2003). Normalization values are from Sun and McDonough (1989). The literature data are the same to Fig. 4.

consistent patterns in the primitive-mantle-normalized trace-element spider diagram (Fig. 6b). The NMQ II granite porphyries, however, have lower Ba, La, Ce, Pr, Sr, P, and Ti contents than the NMQ I samples (Fig. 6b).

4.4. Whole-rock Sr–Nd–Hf isotope geochemistry

Results of Sr–Nd–Hf isotope analyses are given in Supplementary Tables S3 and S4. Initial isotope ratios of the DM, NMQ I, and III granite

porphyries were recalculated using the zircon U–Pb ages obtained in this study. Initial isotope ratios of the NMQ II intrusion were corrected to 79 Ma. The DM intrusion exhibits homogeneous and low $(^{87}Sr/^{86}Sr)_i$ (0.7049–0.7050) ratios, high $\varepsilon_{Nd}(t)$ (1.2–1.6) and $\varepsilon_{Hf}(t)$ (9.9–12.0) values, with young Nd and Hf model ages (T_{DM2}) of 0.78–0.74 Ga and 0.51–0.38 Ga, respectively. Samples from the NMQ III intrusion have slightly higher $(^{87}Sr/^{86}Sr)_i$ ratios (0.7058–0.7067), lower $\varepsilon_{Nd}(t)$ (−1.1 to −0.9) and $\varepsilon_{Hf}(t)$ (7.0–7.4) values, and older Nd and Hf model ages of 0.97–0.95 Ga and 0.70–0.67 Ga, respectively, than those of the DM samples. Samples from the NMQ I and II intrusions show low and consistent $\varepsilon_{Nd}(t)$ (−4.4 to −2.8) and $\varepsilon_{Hf}(t)$ (5.3–6.6) values and Nd and Hf model ages of 1.3–1.1 Ga and 0.81–0.73 Ga, respectively. The $(^{87}Sr/^{86}Sr)_i$ values of the NMQ I intrusive rocks are variable (0.7079 and 0.7165), whereas those of the NMQ II intrusive rocks are low with a narrow range of 0.7025–0.7051.

4.5. In situ zircon Hf–O isotopes

Zircon Hf–O isotope data are presented in Supplementary Table S5. The DM intrusive rocks have high zircon $\varepsilon_{Hf}(t)$ values of 7.4 to 11.5, identical to their whole-rock Hf isotope values (Table S4). The range of $\delta^{18}O$ values is narrow, from 6.27‰ to 7.11‰. Zircon $\varepsilon_{Hf}(t)$ values for the NMQ III intrusive rocks are variable, ranging from 2.39 to 8.44, whereas their $\delta^{18}O$ values are homogeneous (7.27–7.68‰). Zircons from the NMQ I and II intrusive rocks have large variations in both $\varepsilon_{Hf}(t)$ (2.98–6.73) and $\delta^{18}O$ (6.63–9.17‰) values.

5. Discussion

5.1. Petrogenesis

5.1.1. Rock genetic types

The DM–NMQ granite porphyries lack iron-rich mafic silicate minerals, for instance, hedenbergite, ferrohastingsite, and annite, as well as sodic pyroxene (e.g., aegirine) and sodic amphiboles (e.g., arfvedsonite and riebeckite). These porphyries have lower (Zr + Nb + Ce + Y) (<250 ppm) and ($Na_2O + K_2O - CaO$) contents (Fig. 5a), $FeO^t/(FeO^t + MgO)$ ratios (Fig. 5b), and zircon saturation temperatures (644–772 °C, Boehnke et al., 2013) than those of typical A-type granites (Chappell and White, 1992), suggesting that they are not A-type granites.

The DM granite porphyries contain amphibole, have SiO_2 contents of <72 wt%, and are weakly peraluminous with A/CNK ratios of 1.04–1.14, which are identical to those of typical I-type granitoids in the Lachlan Fold Belt (Chappell and White, 1992). Thus the DM granite porphyries are I-type granites. The NMQ granite porphyries are strongly peraluminous with A/CNK ratios of 1.25–1.50 (Table S2). They are all enriched in Na_2O with Na_2O/K_2O ratios of 0.85–3.26, which differs from the typical K-rich S-type granites (Gao et al., 2016). The lack of inherited zircons in the NMQ granite porphyries also suggests that they may not belong to S-type granites, as S-type granites originate from metasedimentary precursors that commonly contain abundant inherited zircons (Jeon et al., 2012). In SiO_2 vs. ($Na_2O + K_2O - CaO$) and SiO_2 vs. $FeO^t/(FeO^t + MgO)$ diagrams (Fig. 5a–b), all of the samples show I-type granite affinity (Frost et al., 2001). Both Th and Y have been proposed to distinguish fractionated I- from S-type granites (Chappell and White, 1992). They are commonly enriched in monazite that generally fractionates from peraluminous melts during the early stage of magmatic evolution, but Th and Y are incompatible in metaluminous melts. Thus, Th and Y abundances are relatively high in I-type granites and low in S-type granites. The NMQ I and II granite porphyries display obviously fractionated geochemical features. They have higher Th (23–41 ppm) and Y (13–16 ppm) contents than those of typical highly fractionated S-type granites in the Himalayan area (Liu et al., 2014b), and similar Th and Y contents to those of highly fractionated I-type granites in the NLS (He et al., 2019; Fig. 5c–d), indicating a close affinity with I-type granites.

In addition, zircon O isotopic compositions can provide a robust means for distinguishing I- and/or S-type granites (Gao et al., 2016; Wu et al., 2006; Zheng et al., 2007). The majority of clastic metasedimentary rocks, excluding volcanogenic metasedimentary rocks, have high $\delta^{18}O$ values of 10–15‰ at amphibolite to granulite facies conditions. For instance, the mean whole-rock $\delta^{18}O$ value of metapelites is 11‰ (Gao et al., 2016), whereas $\delta^{18}O$ values of metaigneous rocks without low-temperature hydrothermal alteration are generally lower than 8‰ (Simon and Lécuyer, 2005). Thus, S-type granites generally have higher $\delta^{18}O$ values relative to I-type granites on account of inheriting the characteristics of the source. Zircons from the DM and NMQ III granite porphyries have relatively low $\delta^{18}O$ values of 6.27–7.68‰ (Fig. S3a, c), whereas zircons from the NMQ I granite porphyries display slightly high $\delta^{18}O$ values of 6.63–9.17‰ (Fig. S3e). All these data fall within the $\delta^{18}O$ field of metaigneous rocks, which indicates that the DM–NMQ granite porphyries belong to I-type granite.

5.1.2. Assimilation and fractional crystallization

The DM–NMQ granite porphyry plutons are unlikely to be affected by crustal contamination for the following evidences: i) each pluton showing a narrow spectrum of whole-rock major and trace elemental and Sr–Nd isotopic compositions (Tables S2 and S3), ii) a lack of detrital zircons, iii) a lack of correlation between $\varepsilon_{Nd}(t)$ values and SiO_2 contents (Fig. 7a), iv) the absence of wall-rock or crustal xenoliths in the field observations. However, samples from the different intrusions show variable REE patterns and a relatively wide range of Sr–Nd–Hf–O isotopic compositions (Fig. 6a; Tables S3–S5), which may indicate different sources and/or different magmatic processes.

The DM–NMQ intrusions are contemporaneous. In contrast to the NMQ granite porphyries, the DM granite porphyries contain amphibole phenocrysts and have the lowest SiO_2 and highest MgO contents (Fig. 8c), and the most depleted Sr–Nd–Hf isotopic compositions. The DM-NMQ intrusions are unlikely to have originated from a common parental magma, although the DM and NMQ III intrusions have similar REE and multi-element patterns (Fig. 6a–b) and exhibit linear trends between SiO_2 and TiO_2, Al_2O_3, and CaO contents (Fig. 8a, d, h). The relatively high TiO_2, Al_2O_3, and P_2O_5 contents and Nb/Ta ratios (Figs. 7c, 8a, b, h) of the NMQ III intrusive rocks and consistent Zr/Hf ratios (Fig. 7d) of the NMQ III and DM granite porphyries do not support the model of fractional crystallization. In addition, both the DM and NMQ III intrusive rocks have weak Eu anomalies (Fig. 6a) and high Zr/Hf ratios that are close to chondrite values (Fig. 7d; Sun and McDonough, 1989), which indicates that they underwent limited magmatic differentiation. The NMQ I and II granite porphyries have higher SiO_2 and lower MgO, $Fe_2O_3^T$, TiO_2, Al_2O_3, P_2O_5, and CaO contents, lower Zr/Hf ratios, and more enriched Nd–Hf isotopic compositions than the DM and NMQ III granite porphyries (Figs. S3, 7d, 8a–d, g–h, 10, 11a–b), implying that they do not have a common source. However, the NMQ I and II intrusions, showing similar Nd–Hf–O isotopic compositions (Figs. 6b, 10, 11a–b), may have a common parental magma. Their relatively low MgO, $Fe_2O_3^T$, TiO_2, Al_2O_3, P_2O_5, CaO, La contents and Nb/Ta, Zr/Hf, $(La/Yb)_N$ ratios and Eu/Eu* values (Figs. 7b, 8a–d, g–h, 9a, and Table S2) may suggest fractional crystallization of feldspar, Fe–Ti-bearing phases (e.g., biotite, ilmenite, and titanite), apatite, zircon, and/or allanite (Gelman et al., 2014; Wu et al., 2003). Moreover, the NMQ II intrusion might have undergone a higher degree of crystal fractionation and late-stage melt–fluid interaction compared with the NMQ I intrusion, based on the following evidences: i) lower K_2O contents and Eu/Eu* values (Figs. 6a, 8e), indicating a greater degree of fractionation of K-feldspar; ii) lower LREE contents and notable REE tetrad effects, with $TE_{1,3}$ values of 1.07–1.17 (Figs. 6a, S4; Wu et al., 2017); and iii) supra-chondritic Y/Ho ratios (Fig. S4a; Bau and Dulski, 1995).

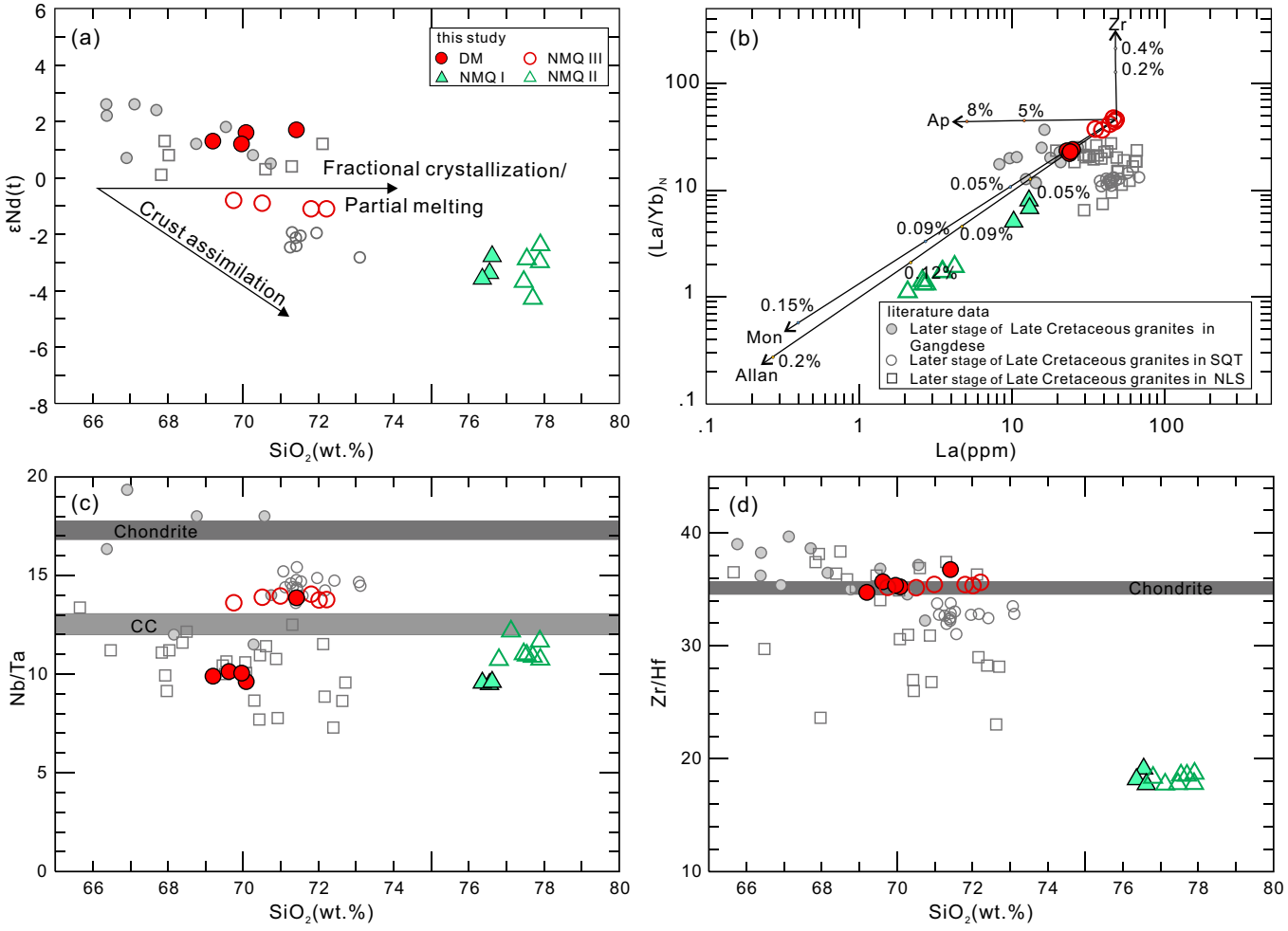

Fig. 7. εNd(t) vs. SiO_2 (a), and $(La/Yb)_N$ vs. La (b), SiO_2 vs. Nb/Ta (c) and Zr/Hf (d) for the Duoma–Namuqie granite porphyries. The source of correlation data is the same of Fig. 4. The data for Chondrite and bulk continental crust (CC) are from Rudnick and Gao (2003) and Sun and McDonough (1989).

5.1.3. Source of the DM–NMQ granite porphyries

Geochemical characteristics suggest that the DM–NMQ granite porphyries have affinity to I-type granites. Several models have been proposed to explain the generation of I-type granites, including i) mafic mineral fractionation at an early stage of evolution of mantle-derived mafic magmas (Chen and Arakawa, 2005), ii) mixing between crust-derived felsic and mantle-derived mafic magmas (Clemens et al., 2009; Wu et al., 2003), and iii) partial melting of the mafic lower continental crust (LCC) (Sisson et al., 2005).

5.1.3.1. DM and NMQ III intrusive rocks. As discussed above, the DM and NMQ III granite porphyries have lower SiO_2 contents and are less differentiated than the NMQ I and II granite porphyries. They have relatively uniform major- and trace-element signatures, and thus cannot have been generated by fractional crystallization of mafic magmas. Magma mixing can generate melts with a wide range of trace-element and isotopic signatures, and may result in the coexistence of different types of zircon with distinct morphologies. The DM and NMQ III granite porphyries have narrow ranges of Sr–Nd–Hf–O isotope compositions and identical zircon type and morphology (Fig. 3a), which suggests that they are unlikely to have been generated by the mixing or mingling of felsic and mafic magmas. This interpretation is supported by the absence of mafic microgranular enclaves in these rocks. Considering their high SiO_2 (69.0–70.0 wt%) contents, they cannot have been produced directly by partial melting of mantle peridotite, which usually yields basaltic melts (Wyllie, 1977). Thus, a possible model for the formation of the DM and NMQ III granite porphyries is partial melting of the LCC, which is favored by the following lines of evidences: i) some major- and trace-element geochemical characteristics are similar to those of the later stage of Late Cretaceous intrusive rocks in the NLS, such as the Rutog adakitic granites (Figs. 6 and 8), which are considered to be formed through partial melting of the thickened LCC (Zhao et al., 2008); ii) the ranges of the Nb/U (2–5), Ce/Pb (2–7), and Th/U (4–7) ratios are similar to those of the LCC (Fig. 9a–b; Foley et al., 2002); iii) as shown in Fig. 9c–d, the DM and NMQ III granite porphyries fall within the field of melts derived by dehydration melting of "amphibolite" that are geochemically equivalent to "metabasites" (Patino Douce, 1999). In addition, Sisson et al. (2005) also proposed that dehydration melting of basaltic to andesitic compositions at pressures of 0.5–1.0 GPa and temperatures of 850–950 °C can generate felsic magmas with SiO_2 contents of >65 wt% and ASI ≥1.0. The high SiO_2 and low HREE contents (Fig. 6a) suggest that the DM granite porphyries could be formed by low degrees of partial melting of basaltic crust (Sisson et al., 2005).

The DM granite porphyries have relatively depleted initial Sr–Nd–Hf isotopic compositions, with low $^{87}Sr/^{86}Sr$ ratios of 0.7049–0.7050, and $\delta^{18}O$ values of 6.3–7.1‰, positive $\varepsilon_{Nd}(t)$ values of 1.2–1.7, and $\varepsilon_{Hf}(t)$ values of 9.9–12.0 for whole rocks and 7.4–11.5 for zircon (Tables S3–S5). These isotopic characteristics are different from those of the Late Jurassic to Early Cretaceous MORB and OIB (Wang et al., 2016), but can be comparable with those of the Late Cretaceous Rutog granites (Zhao et al., 2008) in the NLS, and Langxian granites in the

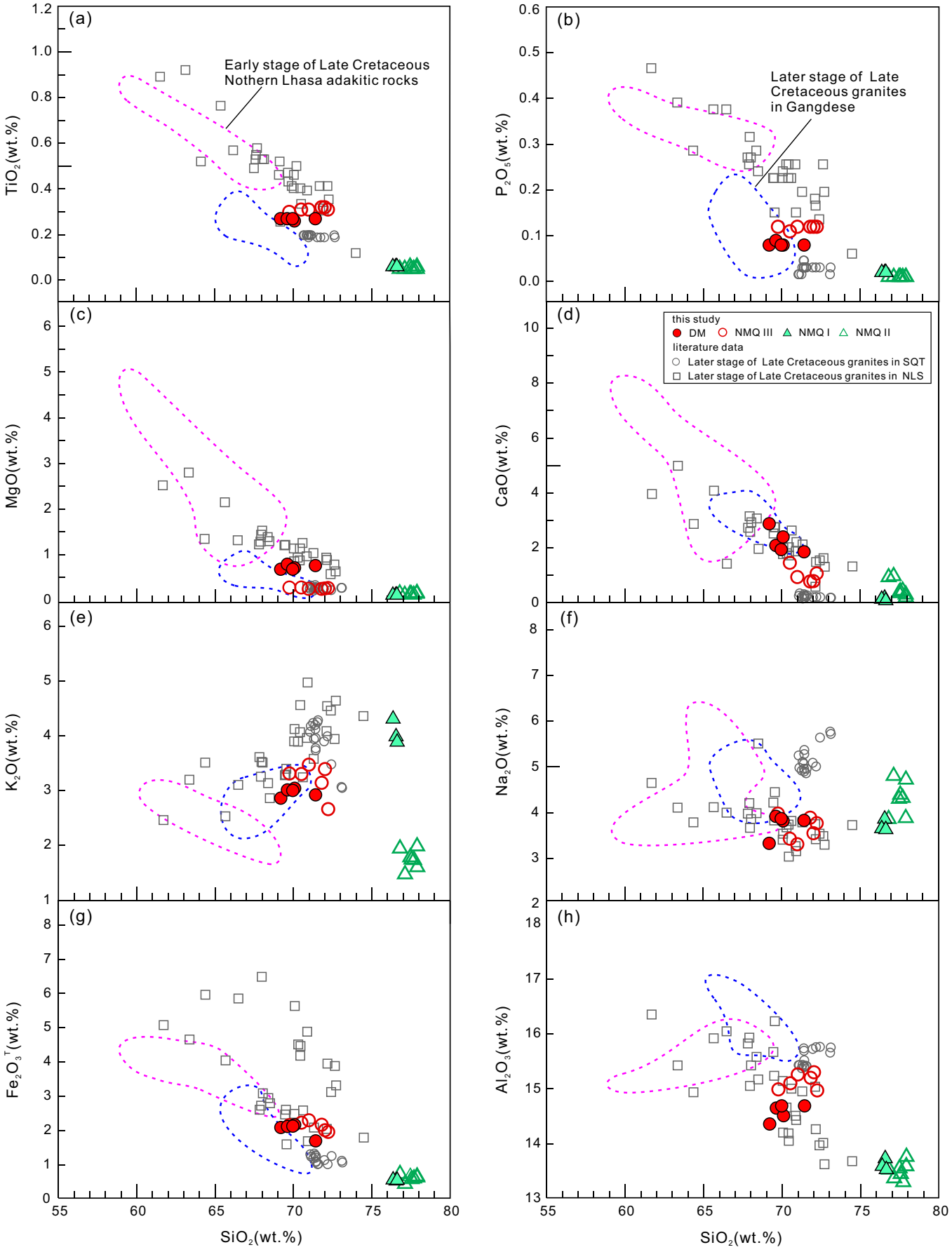

Fig. 8. Selected chemical variation diagrams for the Duoma–Namuqie granite porphyries. The source of correlation data is the same to Fig. 4.

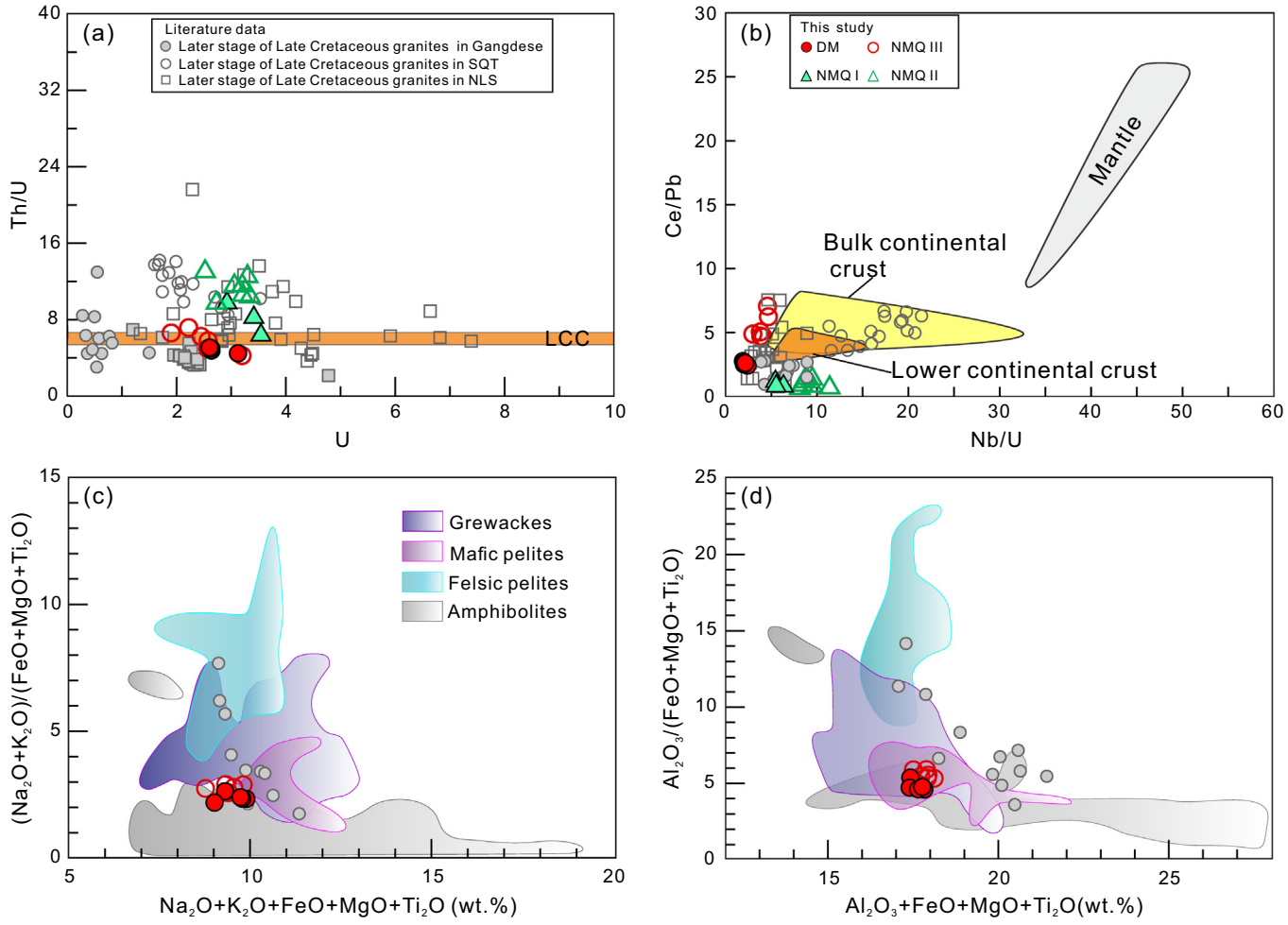

Fig. 9. (a) Th/U vs. U. The average Th/U ratio (~6) of the LCC is from Rudnick and Gao (2003). (b) Ce/Pb vs. Nb/U. The data for mantle, bulk continental crust and LCC are from Rudnick and Gao (2003) and Sun and McDonough (1989). Compositions of the Duoma–Namuqie granite porphyries, compared with experimental melts from a wide range of bulk compositions (Patino Douce, 1999). The source of correlation data is the same of Fig. 5.

Gangdese orogen (Tang et al., 2019b; Fig. 11). This indicates that the DM granite porphyries were generated by partial melting of a juvenile mafic lower crust. Given the young Hf model ages and arc-like geochemical features, namely, enrichment in LILEs and LREEs but depletion in HFSEs and HREEs (Fig. 6a–b), both the subducting Meso-Tethyan oceanic crust and the newly underplated mafic arc crust during the Late

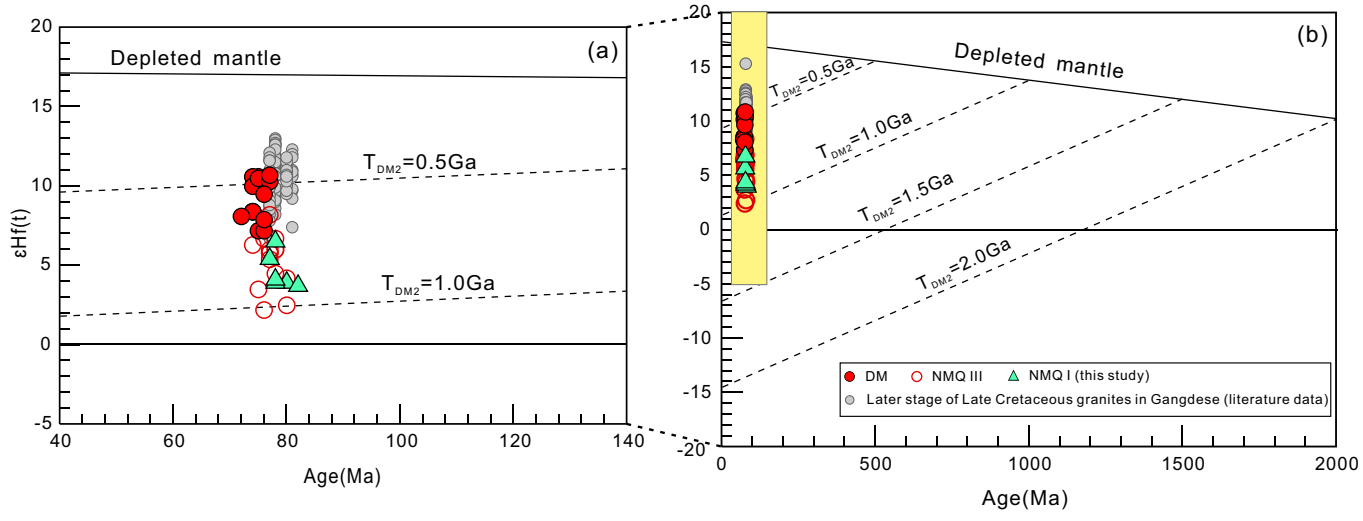

Fig. 10. Relationship between $\varepsilon_{Hf}(t)$ values and U—Pb ages for zircons from the Duoma–Namuqie granite porphyries. Hf isotopic compositions of chondrite and depleted mantle are from Blichert-Toft and Albarède (1997) and Vervoort and Blichert-Toft (1999). Data for the later stage of Late Cretaceous Gangdese granitic rocks are from Tang et al. (2019b).

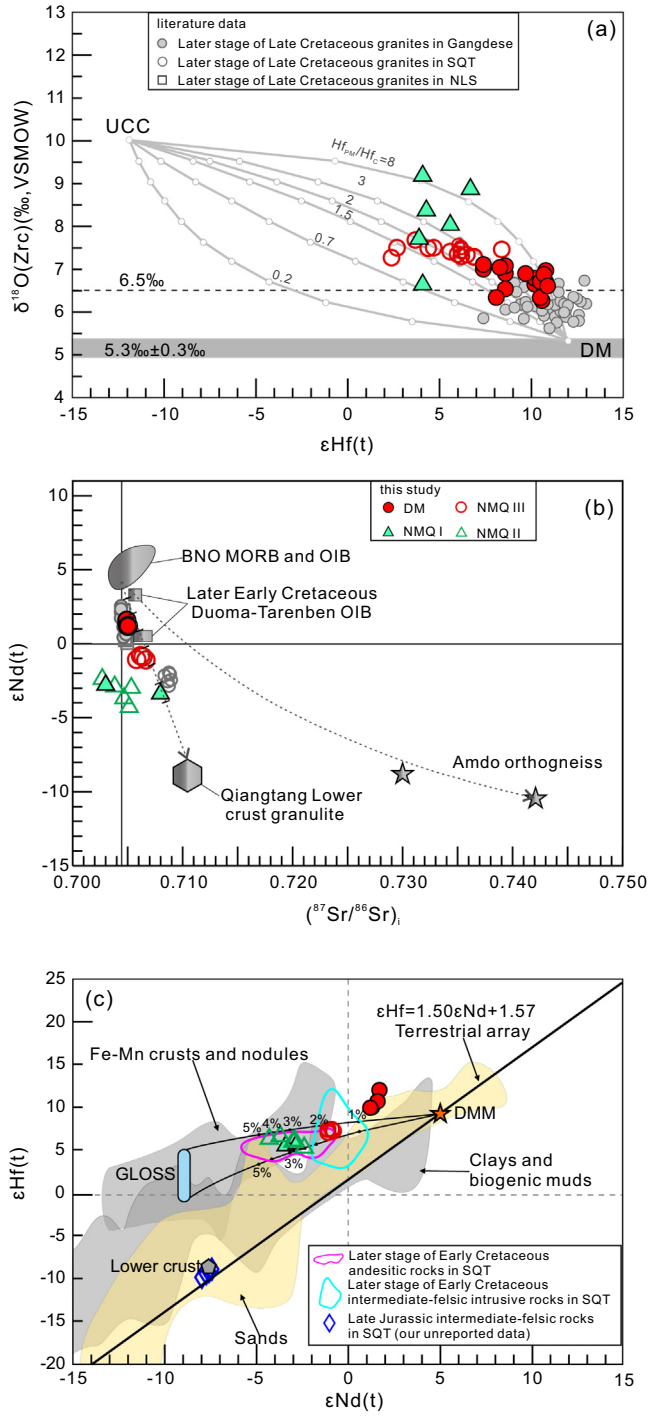

Fig. 11. Zircon $\delta^{18}O$ vs. $\varepsilon_{Hf}(t)$ (a), whole-rock $(^{87}Sr/^{86}Sr)_i$ vs. $\varepsilon_{Nd}(t)$ (b), and $\varepsilon_{Nd}(t)$–$\varepsilon_{Hf}(t)$ diagram for the Duoma–Namuqie granite porphyries. Hf_{pm}/Hf_c is the ratio of Hf concentration in the parental mantle magmas (PM) over crustal (C) melt indicated for each curves and the small circles on the curves represent 10% mixing increments by assuming the mantle zircon has $\varepsilon_{Hf}(t) = 12$ and $\delta^{18}O = 5.3‰$; the supracrustal zircon has $\varepsilon_{Hf}(t) = -12$ and $\delta^{18}O = 10‰$. 6.5‰ represents upper limit of zircon $\delta^{18}O$ that might be accounted for by fractional crystallization (Valley et al., 2005). The end-members of Sr—Nd isotope mixing curves are Bangong–Nujiang Oceanic MORB and OIB (Wang et al., 2016), Qiangtang Lower crust granulite (Lai et al., 2011) and Amdo orthogneiss (Harris et al., 1988). The later stage of Early Cretaceous Duoma–Tarenben OIB (Zhu et al., 2006) is also plotted for comparison. Sources for the literature data: Later stage of Late Cretaceous granites in the SQT, NLS and Gangdese are from He et al. (2019), Tang et al. (2019b) and Zhao et al. (2008), respectively. The Nd and Hf contents of depleted MORB mantle (DMM), global subducting sediment (GLOSS), and lower crust are from Workman and Hart (2005), Rudnick and Gao (2003), and Plank (2014), respectively. The Nd—Hf isotopic compositions of DMM, GLOSS ($\varepsilon_{Nd} = -8.9$, $\varepsilon_{Hf} = +2 \pm 3$), and lower crust are from Li et al. (2016), Chauvel et al. (2008), and Hao et al. (2016), respectively.

Jurassic to Early Cretaceous (Hao et al., 2016; Zhu et al., 2016) are likely candidates for the source rocks of the DM granite porphyries. Partial melting of subducting oceanic crust would produce adakitic magmas, which may not apply to the formation of the DM granite porphyries on account of their low Sr/Y (12–19) ratios. Therefore, the juvenile components in the source could be underplated mafic arc crust. However, the slightly enriched Sr–Nd–Hf isotopes and high $\delta^{18}O$ values of the DM granite porphyries relative to representative depleted-mantle values (Valley et al., 2005; Wang et al., 2016), may indicate a contribution (10%–20%) from ancient crustal materials (Fig. 11a–b). The NMQ III granite porphyries have slightly enriched Sr–Nd–Hf isotopic compositions with neutral $^{87}Sr/^{86}Sr$ ratios of 0.7058–0.7067, $\varepsilon_{Nd}(t)$ values of −1.1 to −0.8, and positive $\varepsilon_{Hf}(t)$ values of 7.0–7.4 for whole rocks and 2.7–9.5 for zircon (Tables S3–S5). These NMQ III rocks may share the same source components as the DM granite porphyries, but involving a greater proportion (20%–40%) of mature crust (Fig. 11a–b). This interpretation is also indicated by their higher zircon $\delta^{18}O$ values (7.3–7.7‰) relative to the depleted-mantle value of 5.3‰ (Valley et al., 2005), as previous studies have suggested that zircons with $\delta^{18}O$ values of >6.5‰ are indicative of significant involvement of supracrustal materials (Hawkesworth et al., 2010; Valley et al., 2005).

5.1.3.2. NMQ I and II intrusions. As discussed above, the NMQ I and II granite porphyries underwent moderate to high degrees of fractional crystallization. However, they cannot have been generated directly by fractional crystallization of mantle-derived mafic magmas or mixing between mafic and felsic magmas, based on the following reasons: i) the extremely high SiO_2 contents (up to >76 wt%), which could not be caused by fractional crystallization of hydrous mafic magmas (Sisson et al., 2005); ii) the lack of corresponding coeval mafic magmas in the surrounding area, and coexisting different types of zircons with distinct morphologies; iii) the relatively uniform Nd–Hf isotope compositions (Fig. 11c). Owing to the influence of hydrothermal alteration, initial Sr isotopes of the NMQ I and II granite porphyries cannot be used as an effective indicator of the source. However, Nd isotopes are not affected by hydrothermal alteration. In addition, magmatic differentiation would have only a limited effect on Sm/Nd ratios, because of the similar geochemical behaviors of Sm and Nd in granitic magmas, which in turn implies a negligible influence of magmatic differentiation on the $\varepsilon_{Nd}(t)$ values of evolved melts. Therefore, Nd isotopes can be used to effectively trace the magma source. Furthermore, zircon Hf–O isotopes have also been widely used to determine the magma source of highly fractionated granites (Li et al., 2009; Valley et al., 2005). This was mainly based on the high closure temperature for Hf and the extremely low diffusivity of O (Bindeman et al., 2013), and the resilience of the systematics of both Hf and O isotopes of zircon to later alteration (Wu et al., 2006; Zheng et al., 2007).

Compared with the NMQ III granite porphyries, the NMQ I and II granite porphyries have more enriched Nd–Hf isotopic compositions (with low whole-rock $\varepsilon_{Nd}(t)$ values of −4.3 to −2.4 and $\varepsilon_{Hf}(t)$ values of 5.3–6.6, and zircon $\varepsilon_{Hf}(t)$ values of 2.98–6.73), higher $\delta^{18}O$ values (7.24–9.17‰), and older whole-rock Hf model ages (810–725 Ma versus 697–673 Ma; Tables S3–S5). The Nd isotopic compositions of the NMQ I and II granite porphyries are more depleted than those of the Amdo orthogenesis and granulite xenoliths in the Qiangtang terrane (Harris et al., 1988; Lai et al., 2011), but are similar to those of the Chuburi granites (ca. 73 Ma; He et al., 2019), Amdo andesites (ca. 80 Ma; Chen et al., 2017), Abushan volcanic rocks (80–76 Ma; Li et al., 2013) in the SQT, and the Zhongcang adakitic rocks (ca. 90 Ma; Yu et al., 2011) that were derived by partial melting of thickened lower crust in the NLS, indicating that the source of these granite porphyries was a mixture of mantle-derived components (~40%) and ancient lower-crustal materials (~60%; Fig. 11b). This interpretation is supported by their positive $\varepsilon_{Hf}(t)$ values and high $\delta^{18}O$ values (Fig. 11a).

In conclusion, the magma sources of the studied granite porphyry intrusions are distinct, with variable degrees of mixing between mantle-

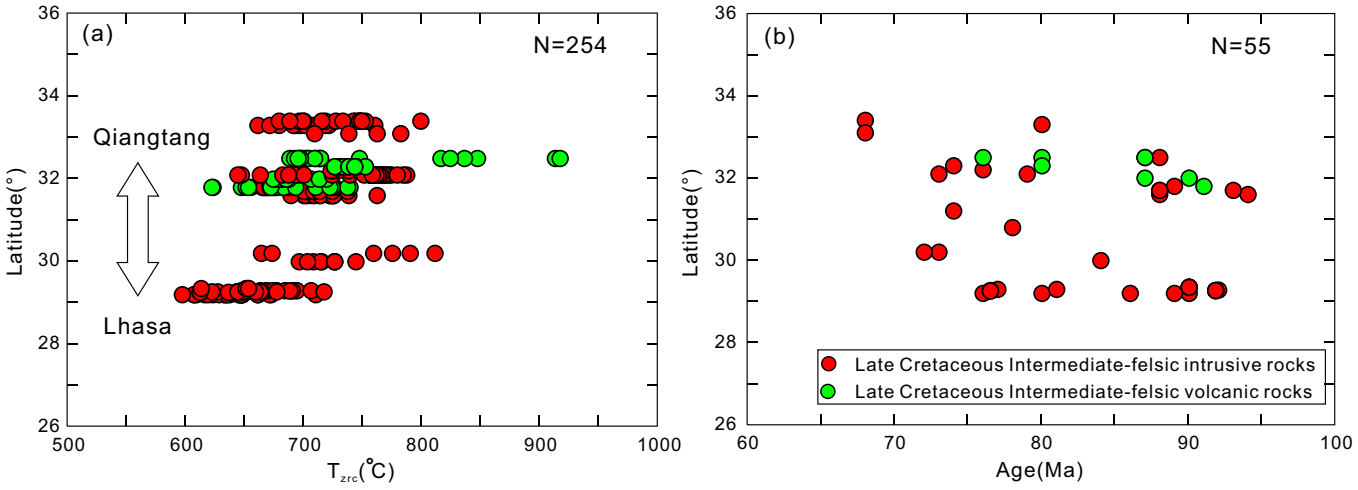

Fig. 12. Whole-rock zircon saturation temperature (a) and Spatial–temporal changes (b) of Late Cretaceous magmatic rocks in Tibet. T_{Zrc} (°C) is calculated after Boehnke et al. (2013). Data sources for the Late Cretaceous intermediate-felsic intrusive and volcanic rocks are listed in Supplementary Table S6.

derived components (40–80%) and mature crustal materials (60–20%). Their different sources might be ascribed to the uneven geometry of the LCC beneath the BNSZ, which could have been caused by collision between the Qiangtang and Lhasa terranes during the late Early Cretaceous (Hao et al., 2019; Li et al., 2017; Zhu et al., 2016).

5.1.4. Nd-–Hf isotope decoupling: A juvenile arc lower-crust source?

All of the DM–NMQ granite porphyries show marked Nd–Hf isotope decoupling, with their whole-rock or zircon $\varepsilon_{Hf}(t)$ values positively deviated from whole-rock $\varepsilon_{Nd}(t)$ values relative to the normal terrestrial arrays of mantle and crust (Vervoort and Blichert-Toft, 1999; Fig. 11c). This isotope pattern may result from disequilibrium melting processes, or inheritance from the magma source (Sun et al., 2021; Tang et al., 2014). Various degrees of zircon dissolution in the source (the "zircon effect") can lead to different Hf isotopic compositions in different batches of melts (Tang et al., 2014). Residual zircons with low Lu/Hf ratios can retain significant ^{177}Hf from the magma source, elevate the $^{176}Hf/^{177}Hf$ ratios of the melts, and result in decoupling of Nd–Hf isotope ratios (Tang et al., 2014). Given that no zircon xenocrysts or significant Zr depletion were observed in the DM–NMQ granite porphyries (Fig. 6b), the Nd–Hf isotope decoupling cannot be explained by disequilibrium melting of the source, but instead by inheritance from the magma source.

Abnormal enrichment of radiogenic Hf isotopes in terrestrial rocks is typically related to anomalously high Lu/Hf ratios in their source. As discussed above, the magma source of the DM–NMQ granite porphyries was composed predominantly of mantle-derived components (40–80%) and lesser proportions (60–20%) of ancient crustal materials. A previous study has proposed that a garnet-rich source may provide very high radiogenic $^{176}Hf/^{177}Hf$ ratios over time, owing to the very high Lu/Hf ratios in garnet. Although the DM and NMQ III granite porphyries are depleted in HREEs relative to contemporary granites in the NLS and SQT (Fig. 6a), the relatively flat HREE pattern is inconsistent with the presence of residual garnet in their source (Fig. 6a). The above points together suggest that the depleted components in the source of the DM–NMQ granite porphyries could be juvenile arc lower crust that was formed by partial melting of the metasomatized mantle wedge. These granite porphyries might have inherited the Nd–Hf isotopic decoupling feature of the mantle as a result of metasomatization by subducted-sediment melts (Sun et al., 2021). During hydrous melting of the subducted sediments, monazite would have preferentially broken down and released Nd, whereas zircon, with significant Hf, was able to remain in the residue under high temperature (~1000 °C) (Hermann and Rubatto, 2009), which would have resulted in high Nd/Hf ratios in the melt, and finally leading to Nd–Hf isotope decoupling within the mantle (Todd et al., 2010). Alternatively, the involvement of ancient crustal basement with high Lu/Hf ratios can also explain Nd–Hf

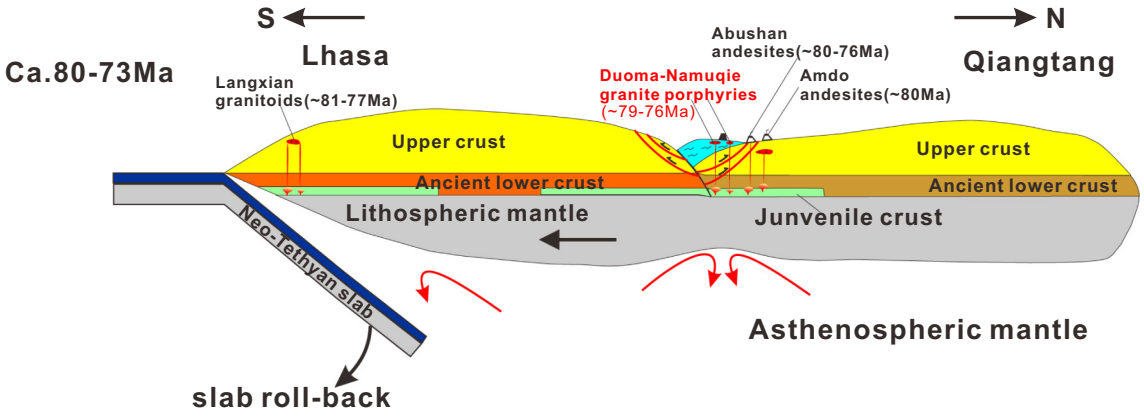

Fig. 13. A model for Late Cretaceous transtension in Tibet and the generation of the Duoma–Namuqie granite porphyries. Not to scale. Age data for Langxian granitoids, Amdo and Abushan andesites are from Tang et al. (2019b), Chen et al. (2017), and Li et al. (2013), respectively.

isotope decoupling (Chauvel et al., 2009; Vervoort and Blichert-Toft, 1999). However, granulite xenoliths in the Qiangtang block (Lai et al., 2011), a possible source of ancient crust, have low Lu/Hf ratios that range mostly from 0.056 to 0.079, similar to the average crustal composition (Rudnick and Fountain, 1995). Furthermore, the intrusions that were derived by partial melting of the ancient lower crust in the SQT show coupled Nd–Hf isotopic compositions (Sun et al., 2021; Fig.11c). Both of these points rule out the effects of involving ancient lower crust on the Nd–Hf isotope decoupling in the DM–NMQ granite porphyries. Therefore, the decoupled Nd–Hf isotope systematics point to a likely source of juvenile arc lower crust for the DM–NMQ granite porphyries.

In conclusion, the Nd–Hf–O isotope data obtained in this study indicate that the DM–NMQ granite porphyries were mainly produced by rapid partial melting of pre-existing juvenile arc crust. Such a process possibly played an important role in intra-crustal differentiation. In addition, the involvement of small to moderate amounts of ancient continental materials in their magma source accelerated the maturation of the continental crust.

5.2. Geodynamic processes

5.2.1. Late Cretaceous magmatism in the Lhasa and Qiangtang terranes

Numerous Late Cretaceous and Early Paleocene (100–64 Ma) intermediate–felsic rocks are distributed in the Lhasa terrane (Fig. 1a). Magmatic activity in the central and northern Lhasa subterranes occurred mostly during the early stage of Late Cretaceous (94–85 Ma), including the generation of the Baingoin adakitic dikes (ca. 94 Ma; Yi et al., 2018), Zhuogapu Mg-rich andesites and dacites (ca. 91 Ma; Wang et al., 2014), Zhongcang high-Mg adakitic granitoids (ca. 91–88 Ma; Chen et al., 2015; Yu et al., 2011), high-Mg adakitic rhyodacites/dacites in Azhang (ca. 90–87 Ma; Sun et al., 2015), and high-Mg adakitic quartz diorites in Gaerqiong (ca. 90–88 Ma; Li et al., 2017; Lei et al., 2015). These magmatic rocks with adakitic and high-Mg signatures are recognized as the products of lithospheric foundering after collision between the Lhasa and Qiangtang terranes. Magmatic rocks that were formed during the later stage of Late Cretaceous are sporadic and include the Rutog high-Mg adakitic granitoids (ca. 80 Ma; Zhao et al., 2008) and ore-related granites (80–76 Ma; Ding et al., 2012) in the Baingoin area. Late Cretaceous magmatism in southern Lhasa are concentrated in the central–eastern part of that subterrane (Zhu et al., 2018; Fig. 1a). The early-stage magmatism (100–85 Ma) is dominated by mafic and adakitic rocks, charnockites, and a few highly fractionated leucogranites associated with Neo-Tethyan ridge subduction (Zhu et al., 2018) or subducting-slab roll-back (Ma et al., 2013a, 2013b), whereas the late-stage magmatism (85–70 Ma) is represented by felsic rocks, chiefly the Langxian granites (Tang et al., 2019b), which were generated by reworking of pre-existing juvenile crust during flat subduction of the Neo-Tethyan oceanic slab (Tang et al., 2019b; Zhu et al., 2018).

Small volumes of Late Cretaceous magmatic rocks have been found in the Qiangtang terrane and are mainly distributed in the south of the terrane along the BNSZ from Rotug to Changdu (Fig. 1a). Most of the magmatic rocks were formed during the later stage of Late Cretaceous (80–68 Ma), including potassium-rich andesites–trachyandesites (80–76 Ma) in the DM and Amdo areas, which were produced by partial melting of mafic lower crust or metasomatized lithospheric mantle (Chen et al., 2017; Li et al., 2013), Chuburi highly fractionated I-type granites (ca. 73 Ma) in the Amdo area, which are regarded as products of melting of the lower crust (He et al., 2019), and the Munai K-rich charnockite–granite suit (ca. 68 Ma) in the Yanshiping area formed by partial melting of a thickened lower crust (Lu et al., 2019). The petrogenesis of these magmatic rocks constrains the post-collision period involving the Lhasa and Qiangtang terranes. The early stage of Late Cretaceous magmatism in the SQT is mainly represented by the Biluoco magnesian andesites (ca. 95 Ma; He et al., 2018) and the Gaize bimodal basalt–rhyolite suite (97–87 Ma; Liu et al., 2018), which have been recognized as a delayed response to slab break-off from the northward-subducting Bangong–Nujiang oceanic lithosphere at ca. 100 Ma.

5.2.2. Geodynamic processes

The Late Cretaceous was an important geological interval for the Tibetan Plateau because it corresponds to the time during which the tectonic regime changed from Lhasa–Qiangtang terrane collision to Indian–Asian continent assembly. Widespread Late Cretaceous and Early Paleocene (100–64 Ma) magmatism has been found in both the Lhasa and Qiangtang terranes (Fig. 1a). However, the nature of the tectonic regime that controlled the generation of the magma remains unclear.

The BNTO might have undergone diachronous closure. Closure of the western and western-central parts of the BNTO could have occurred after the Late Cretaceous (Hao et al., 2019; Zhang et al., 2012, 2014), based on the discovery of the later stage of Early Cretaceous oceanic islands and volcanic rock suites within the BNSZ. Nevertheless, its eastern segment might have closed during the later stage of Early Cretaceous (Kapp et al., 2007; Zhu et al., 2016). The subsequent Lhasa–Qiangtang collision, together with the accretion of the Meso-Tethys oceanic plateau, could have caused significant crustal thickening (Zhang et al., 2014). The Amdo andesites (ca. 80 Ma) with high La/Yb ratios, the 80 Ma Rutog adakitic granite, and 91–88 Ma adakites in the Zhongcang and Nyima regions reflect the presence of a thickening lithosphere beneath central Tibet during the Late Cretaceous (Chen et al., 2015; Chen et al., 2017; Wang et al., 2014; Yu et al., 2011; Zhao et al., 2008). This thickening is also supported by sedimentological and structural studies, which have shown that central Tibet underwent significant N–S shortening during the Late Cretaceous (Kapp et al., 2007). The presence of 80–76 Ma Abushan volcanic rocks, 78–74 Ma peraluminous A-type granite and metaluminous syenite in the eastern BNSZ, 68 Ma Munai charnockite, and 73 Ma Chuburi highly differentiated I-type granite is consistent with extension during the later stage of Late Cretaceous in central Tibet (He et al., 2019; Li et al., 2013; Lu et al., 2019). The 79–76 Ma DM–NMQ granite porphyries are likely to have been formed in a post-collisional extensional environment. However, the nature of the extensional regime continues to be vigorously debated. In accordance with the inferred crustal thickening during the early stage of Late Cretaceous, a prevalent model involving lithospheric delamination has been proposed to explain the extension in the Qiangtang terrane (He et al., 2019; Li et al., 2013; Lu et al., 2019). Recently, some studies have suggested that the extension could have been driven by the far-field effects of subduction of the Neo-Tethys oceanic crust (Chapman et al., 2018; Wang et al., 2019). Considering the sudden change in geodynamic setting at the end of the Early Cretaceous and the development of two Late Cretaceous igneous belts along strike-slip faults in the eastern Qiangtang terrane, Wang et al. (2019) proposed an episode of transtension between the Lhasa and Qiangtang terranes triggered by Meso-Tethyan slab break-off at around 110 Ma and subsequently by the far-field effects of subduction of the Neo-Tethys oceanic crust during the later stage of Late Cretaceous. Late Cretaceous magmatism (80–70 Ma) in the central and northern South Pamir terranes, the western extension of the Qiangtang terrane, was interpreted as a result of extension associated with roll-back of the Neo-Tethyan oceanic slab (Chapman et al., 2018).

We suggest that the later stage of Late Cretaceous extension along the BNSZ could have been related to roll-back of the Neo-Tethyan oceanic slab, on the basis of the following evidences. First, the Late Cretaceous magmatic rocks in the SQT and NLS are scattered and small in volume. Second, the Late Cretaceous magmatism is dominated by intermediate–felsic rocks and lacks mafic rocks. Both of these features are distinct from the late Mesozoic magmatism in eastern Yangtze, which is characterized by widespread adakitic rocks, I- and A-type granites, and shoshonitic igneous rocks that are considered to have been formed in an extensional setting as a result of lithospheric delamination

(Wang et al., 2006a, 2006b). Third, statistical data show that the Late Cretaceous magmatic rocks trend N–S, from the SQT to the Gangdese zone, and most of these rocks are felsic and were formed at low to moderate magmatic temperatures (~597 to 917 °C) (Fig. 12a–b), which indicates that their formation could have been controlled by similar kinetic mechanism. The Neo-Tethyan oceanic slab might have undergone a model transition from ridge subduction during the early stage of Late Cretaceous (100–85 Ma; Zhang et al., 2010; Zhu et al., 2013) to slab roll-back during the later stage of Late Cretaceous and Early Paleocene (85–62 Ma; Chapman et al., 2018; Ma et al., 2013a, 2013b). Responding to this kinematic regime, the Meso-Tethyan oceanic slab might have undergone an early stage of post-collisional compression during the early stage of Late Cretaceous (100–80 Ma) and a later stage of extension (80–68 Ma). Therefore, the later stage of Late Cretaceous extension along the BNSZ could have been triggered by the far-field effect of Neo-Tethyan slab roll-back, which might have caused thermal disturbance of the mantle and induced asthenospheric upwelling. This process could have triggered the reactivation of the BNSZ and resulted in the partial melting of juvenile arc lower crust (Fig. 13).

6. Conclusions

(1) Zircon SIMS U–Pb dating indicates that the Duoma–Namuqie (DM–NMQ) granite porphyries in the southern Qiangtang subterrane near the Bangong–Nujiang suture zone were emplaced at 79–76 Ma.
(2) The DM–NMQ granite porphyries were mainly produced by rapid partial melting of pre-existing juvenile arc crust, which contributed to intra-crustal differentiation, and involvement of small to moderate amounts of ancient continental materials in their magma source accelerated maturation of the continental crust.
(3) The DM–NMQ granite porphyries were formed in a post-collisional extensional setting, possibly triggered by the far-field effects of the subduction of the Neo-Tethyan oceanic crust.

Declaration of Competing Interest

The authors declare that they have no known competing financial interests or personal relationships that could have appeared to influence the work reported in this paper.

Acknowledgments

We are grateful to Editor Professor Xian-Hua Li, and two anonymous reviewers for their constructive review comments. We sincerely appreciate the assistance of Sheng-ling Sun, Xiang-Ling Tu, Wen Zeng, Xiao-Ping Xia, Ya-Nan Yang and Le Zhang for the geochemical analyses and zircon U–Pb age dating. Financial support for this research was provided by the National Natural Science Foundation of China (Nos. 41630208, 42021002 and 91855215), the National Key R & D Program of China (No. 2016YFC0600407), the Second Tibetan Plateau Scientific Expedition and Research (STEP) (2019QZKK0702), and the Strategic Priority Research Program (A) of the Chinese Academy of Sciences (No. XDA2007030402). This is contribution No. IS–2993 from GIGCAS.

Appendix A. Supplementary data

Supplementary data to this article can be found online at https://doi.org/10.1016/j.lithos.2021.106097.

References

Bau, M., Dulski, P., 1995. Comparative study of yttrium and rare-earth element behaviours in fluorine-rich hydrothermal fluids. Contrib. Mineral. Petrol. 119, 213–223.
Bindeman, I., Schmitt, A., Lundstrom, C., Golledge, S., 2013. Long-term (4 mo) oxygen isotope exchange experiment between zircon and hydrothermal fluid. AGUFM 2013, V53B–2798.
Blichert-Toft, J., Albarède, F., 1997. The Lu-Hf isotope geochemistry of chondrites and the evolution of the mantle-crust system. Earth Planet. Sci. Lett. 148, 243–258.
Boehnke, P., Watson, E.B., Trail, D., Harrison, T.M., Schmitt, A.K., 2013. Zircon saturation revisited. Chem. Geol. 351, 324–334.
Chapman, J.B., Scoggin, S.H., Kapp, P., Carrapa, B., Ducea, M.N., Worthington, J., Oimahmadov, I., Gadoev, M., 2018. Mesozoic to Cenozoic magmatic history of the Pamir. Earth Planet. Sci. Lett. 482, 181–192.
Chappell, B., White, A., 1992. I-and S-type granites in the Lachlan Fold Belt. Trans. R. Soc. Edinb. Earth Sci. 83, 1–26.
Chauvel, C., Lewin, E., Carpentier, M., Arndt, N.T., Marini, J.C., 2008. Role of recycled oceanic basalt and sediment in generating the Hf–Nd mantle array. Nat. Geosci. 1, 64.
Chauvel, C., Marini, J.C., Plank, T., Ludden, J.N., 2009. Hf-Nd input flux in the Izu-Mariana subduction zone and recycling of subducted material in the mantle. Geochem. Geophys. Geosyst. 10.
Chen, B., Arakawa, Y., 2005. Elemental and Nd–Sr isotopic geochemistry of granitoids from the West Junggar foldbelt (NW China), with implications for Phanerozoic continental growth. Geochim. Cosmochim. Acta 69, 1307–1320.
Chen, J.L., Xu, J.F., Yu, H.X., Wang, B.D., Wu, J.B., Feng, Y.X., 2015. Late cretaceous high-Mg# granitoids in southern Tibet: Implications for the early crustal thickening and tectonic evolution of the Tibetan Plateau? Lithos 232, 12–22.
Chen, S.S., Fan, W.M., Shi, R.D., Gong, X.H., Wu, K., 2017. Removal of deep lithosphere in ancient continental collisional orogens: a case study from Central Tibet, China. Geochem. Geophys. Geosyst. 18, 1225–1243.
Clemens, J., Darbyshire, D., Flinders, J., 2009. Sources of post-orogenic calcalkaline magmas: the Arrochar and Garabal Hill–Glen Fyne complexes, Scotland. Lithos 112, 524–542.
Ding, L., Zhao, Y.Y., Yang, Y.Q., Cui, Y.B., Lue, L.N., 2012. LA-ICP-MS zircon U-Pb dating and geochemical characteristics of ore-bearing granite in skarn-type iron polymetallic deposits of Duoba area, Baingoin County, Tibet, and their significance. Acta Petrol. Mineral. 31, 479–496 (in Chinese with English abstract).
Foley, S., Tiepolo, M., Vannucci, R., 2002. Growth of early continental crust controlled by melting of amphibolite in subduction zones. Nature 417, 837–840.
Frost, B.R., Barnes, C.G., Collins, W.J., Arculus, R.J., Ellis, D.J., Frost, C.D., 2001. A geochemical classification for granitic rocks. J. Petrol. 42, 2033–2048.
Gao, P., Zheng, Y.F., Zhao, Z.F., 2016. Distinction between S-type and peraluminous I-type granites: Zircon versus whole-rock geochemistry. Lithos 258, 77–91.
Gelman, S.E., Deering, C.D., Bachmann, O., Huber, C., Gutierrez, F.J., 2014. Identifying the crystal graveyards remaining after large silicic eruptions. Earth Planet. Sci. Lett. 403, 299–306.
Hao, L.L., Wang, Q., Wyman, D.A., Ou, Q., Dan, W., Jiang, Z.Q., Wu, F.Y., Yang, J.H., Long, X.P., Li, J., 2016. Underplating of basaltic magmas and crustal growth in a continental arc: evidence from late Mesozoic intermediate–felsic intrusive rocks in southern Qiangtang, Central Tibet. Lithos 245, 223–242.
Hao, L.L., Wang, Q., Zhang, C., Ou, Q., Yang, J.H., Dan, W., Jiang, Z.Q., 2019. Oceanic plateau subduction during closure of the Bangong–Nujiang Tethyan Ocean: Insights from central Tibetan volcanic rocks. Geol. Soc. Am. Bull. 131, 864–880.
Harris, N., Ronghua, X., Lewis, C., Hawkesworth, C.J., Yuquan, Z., 1988. Isotope geochemistry of the 1985 Tibet geotraverse, Lhasa to Golmud. Philosophical transactions of the Royal Society of London. Series a. Math. Phys. Sci. 327, 263–285.
Hawkesworth, C., Turner, S., McDermott, F., Peate, D., Van Calsteren, P., 1997. U–Th isotopes in arc magmas: Implications for element transfer from the subducted crust. Science 276, 551–555.
Hawkesworth, C.J., Dhuime, B., Pietranik, A., Cawood, P., Kemp, A.I., Storey, C., 2010. The generation and evolution of the continental crust. J. Geol. Soc. 167, 229–248.
He, H.Y., Li, Y.L., Wang, C.S., Zhou, A., Qian, X.Y., Zhang, J.W., Du, L.T., Bi, W.J., 2018. Late cretaceous (ca. 95 Ma) magnesian andesites in the Biluoco area, southern Qiangtang subterrane, Central Tibet: Petrogenetic and tectonic implications. Lithos 302, 389–404.
He, H.Y., Li, Y.L., Wang, C.S., Han, Z.P., Ma, P.F., Xiao, S.Q., 2019. Petrogenesis and tectonic implications of late cretaceous highly fractionated I-type granites from the Qiangtang block, Central Tibet. J. Asian Earth Sci. 176, 337–352.
Hermann, J., Rubatto, D., 2009. Accessory phase control on the trace element signature of sediment melts in subduction zones. Chem. Geol. 265, 512–526.
Hu, W.L., Wang, Q., Yang, J.H., Zhang, C., Tang, G.J., Ma, L., Qi, Y., Yang, Z.Y., Sun, P., 2019. Late early cretaceous peraluminous biotite granites along the Bangong–Nujiang suture zone, Central Tibet: Products derived by partial melting of metasedimentary rocks? Lithos 344, 147–158.
Jeon, H., Williams, I.S., Chappell, B.W., 2012. Magma to mud to magma: Rapid crustal recycling by Permian granite magmatism near the eastern Gondwana margin. Earth Planet. Sci. Lett. 319, 104–117.
Kapp, P., DeCelles, P.G., Gehrels, G.E., Heizler, M., Ding, L., 2007. Geological records of the Lhasa–Qiangtang and Indo–Asian collisions in the Nima area of Central Tibet. Geol. Soc. Am. Bull. 119, 917–933.
Lai, S., Qin, J., Grapes, R., 2011. Petrochemistry of granulite xenoliths from the Cenozoic Qiangtang volcanic field, northern Tibetan Plateau: implications for lower crust composition and genesis of the volcanism. Int. Geol. Rev. 53, 926–945.
Lei, M., Chen, J.L., Xu, J.F., Zeng, Y.C., 2015. Geochemistry of early late cretaceous Gaerqiong high-Mg# diorite porphyry in mid-northern Lhasa terrane: Partial melting of delaminated lower continental crust. Geol. Bull. China 34, 337–346.
Leier, A.L., DeCelles, P.G., Kapp, P., Gehrels, G.E., 2007. Lower cretaceous strata in the Lhasa Terrane, Tibet, with implications for understanding the early tectonic history of the Tibetan Plateau. J. Sediment. Res. 77, 809–825.

Li, C., Zhai, Q.G., Dong, Y.S., Huang, X.P., 2006. Discovery of eclogite and its geological significance in Qiangtang area, Central Tibet. Chin. Sci. Bull. 51, 1095–1100.
Li, X.H., Li, W.X., Wang, X.C., Li, Q.L., Liu, Y., Tang, G.Q., 2009. Role of mantle-derived magma in genesis of early Yanshanian granites in the Nanling Range, South China: in situ zircon Hf–O isotopic constraints. Sci. China Ser. D Earth Sci. 52, 1262–1278.
Li, Y.L., He, J., Wang, C.C., Santosh, M., Dai, J.G., Zhang, Y.X., Wei, Y.S., Wang, J.G., 2013. Late cretaceous K-rich magmatism in Central Tibet: evidence for early elevation of the Tibetan plateau? Lithos 160, 1–13.
Li, G.M., Qin, K.Z., Li, J.X., Evans, N.J., Zhao, J.X., Cao, M.J., Zhang, X.N., 2017. Cretaceous magmatism and metallogeny in the Bangong–Nujiang metallogenic belt, Central Tibet: evidence from petrogeochemistry, zircon U–Pb ages, and Hf–O isotopic compositions. Gondwana Res. 41, 110–127.
Li, S.M., Zhu, D.C., Wang, Q., Zhao, Z., Zhang, L.L., Liu, S.A., Chang, Q.S., Lu, Y.H., Dai, J.G., Zheng, Y.C., 2016. Slab-derived adakites and subslab asthenosphere-derived OIB-type rocks at 156±2 Ma from the north of Gerze, central Tibet: Records of the Bangong–Nujiang oceanic ridge subduction during the Late Jurassic. Lithos 262, 456–469.
Liu, D.L., Huang, Q.S., Fan, S.Q., Zhang, L.Y., Shi, R.D., Ding, L., 2014a. Subduction of the Bangong–Nujiang Ocean: constraints from granites in the Bangong Co area, Tibet. Geol. J. 49, 188–206.
Liu, Z.C., Wu, F.Y., Ji, W.Q., Wang, J.G., Liu, C.Z., 2014b. Petrogenesis of the Ramba leucogranite in the Tethyan Himalaya and constraints on the channel flow model. Lithos 208–209, 118–136.
Liu, D.L., Shi, R.D., Ding, L., Zou, H.B., 2018. Late cretaceous transition from subduction to collision along the Bangong-Nujiang Tethys: New volcanic constraints from Central Tibet. Lithos 296, 452–470.
Lu, L., Zhang, K.J., Jin, X., Zeng, L., Yan, L.L., Santosh, M., 2019. Crustal Thickening of the Central Tibetan Plateau prior to India–Asia Collision: evidence from Petrology, Geochronology, Geochemistry and Sr–Nd–Hf Isotopes of a K-rich Charnockite–Granite Suite in Eastern Qiangtang. J. Petrol. 60, 827–854.
Ma, L., Wang, Q., Wyman, D.A., Jiang, Z.Q., Yang, J.H., Li, Q.L., Gou, G.N., Guo, H.F., 2013a. Late cretaceous crustal growth in the Gangdese area, southern Tibet: petrological and Sr–Nd–Hf–O isotopic evidence from Zhengga diorite–gabbro. Chem. Geol. 349, 54–70.
Ma, L., Wang, Q., Wyman, D.A., Li, Z.X., Jiang, Z.Q., Yang, J.H., Gou, G.N., Guo, H.F., 2013b. Late cretaceous (100–89 Ma) magnesian charnockites with adakitic affinities in the Milin area, eastern Gangdese: Partial melting of subducted oceanic crust and implications for crustal growth in southern Tibet. Lithos 175, 315–332.
Niu, Y.L., Zhao, Z.D., Zhu, D.C., Mo, X.X., 2013. Continental collision zones are primary sites for net continental crust growth—a testable hypothesis. Earth Sci. Rev. 127, 96–110.
Patino Douce, A.E., 1999. What do experiments tell us about ~ the relative contributions of crust and mantle to the origin of granitic magmas? In: Castro, A., Fernandez, C., Vigneresse, J.L. (Eds.), Understanding Granites: Integrating New and Classical Techniques. Geological Society, London, Special Publications vol. 168, pp. 55–75
Plank, T., 2014. The Chemical Composition of Subducting Sediments. Elsevier.
Rudnick, R.L., Fountain, D.M., 1995. Nature and composition of the continental crust: a lower crustal perspective. Rev. Geophys. 33, 267–309.
Rudnick, R., Gao, S., 2003. Composition of the continental crust. The Crust 3, 1–64.
Schneider, W., Mattern, F., Wang, P., Li, C., 2003. Tectonic and sedimentary basin evolution of the eastern Bangong–Nujiang zone (Tibet): a Reading cycle. Int. J. Earth Sci. 92, 228–254.
Simon, L., Lécuyer, C., 2005. Continental recycling: the oxygen isotope point of view. Geochem. Geophys. Geosyst. 6.
Sisson, T., Ratajeski, K., Hankins, W., Glazner, A.F., 2005. Voluminous granitic magmas from common basaltic sources. Contrib. Mineral. Petrol. 148, 635–661.
Sun, S.S., McDonough, W.F., 1989. Chemical and isotopic systematics of oceanic basalts: implications for mantle composition and processes. Geol. Soc. Lond., Spec. Publ. 42, 313–345.
Sun, G.Y., Hu, X.M., Sinclair, H.D., Marcelle, B.D., Wang, J.G., 2015. Late cretaceous evolution of the Coqen basin (Lhasa terrane) and implications for early topographic growth on the Tibetan Plateau. Geol. Soc. Am. Bull. 127 (7–8), 1001–1020.
Tang, M., Wang, X.L., Shu, X.J., Wang, D., Yang, T., Gopon, P., 2014. Hafnium isotopic heterogeneity in zircons from granitic rocks: Geochemical evaluation and modeling of "zircon effect" in crustal anatexis. Earth Planet. Sci. Lett. 389, 188–199.
Tang, G.J., Wang, Q., Wyman, D.A., Dan, W., 2019a. Crustal maturation through chemical weathering and crustal recycling revealed by Hf–O–B isotopes. Earth Planet. Sci. Lett. 524, 115709.
Sun, P., Wang, Q., Hao, L.L., Dan, W., Ou, Q., Jiang, Z.Q., Tang, G.J., 2021. A mélange contribution to arc magmas recorded by Nd-Hf isotopic decoupling: an example from southern Qiangtang Block, Central Tibet. J. Asian. Earth. Sci. (in Review).
Tang, Y.W., Chen, L., Zhao, Z.F., Zheng, Y.F., 2019b. Geochemical evidence for the production of granitoids through reworking of the juvenile mafic arc crust in the Gangdese orogen, southern Tibet. Geol. Soc. Am. Bull. 132, 1347–1364.
Todd, E., Gill, J., Wysoczanski, R., Handler, M.R., Wright, I., Gamble, J., 2010. Sources of constructional cross-chain volcanism in the southern Havre Trough: New insights from HFSE and REE concentration and isotope systematics. Geochem. Geophys. Geosyst. 11.
Valley, J., Lackey, J., Cavosie, A., Clechenko, C., Spicuzza, M., Basei, M., Bindeman, I., Ferreira, V., Sial, A., King, E., 2005. 4.4 billion years of crustal maturation: oxygen isotope ratios of magmatic zircon. Contrib. Mineral. Petrol. 150, 561–580.
Vervoort, J.D., Blichert-Toft, J., 1999. Evolution of the depleted mantle: Hf isotope evidence from juvenile rocks through time. Geochim. Cosmochim. Acta 63, 533–556.
Wang, Q., Wyman, D.A., Xu, J.F., Zhao, Z.H., Jian, P., Xiong, X.L., Bao, Z.W., Li, C.F., Bai, Z.H., 2006a. Petrogenesis of cretaceous adakitic and shoshonitic igneous rocks in the Luzong area, Anhui Province (eastern China): implications for geodynamics and Cu–au mineralization. Lithos 89, 424–446.
Wang, Q., Xu, J.F., Jian, P., Bao, Z.W., Zhao, Z.H., Li, C.F., Xiong, X.L., Ma, J.L., 2006b. Petrogenesis of adakitic porphyries in an extensional tectonic setting, Dexing, South China: implications for the genesis of porphyry copper mineralization. J. Petrol. 47, 119–144.
Wang, Q., Zhu, D.C., Zhao, Z.D., Liu, S.A., Chung, S.L., Li, S.M., Liu, D., Dai, J.G., Wang, L.Q., Mo, X.X., 2014. Origin of the ca. 90 Ma magnesia-rich volcanic rocks in SE Nyima, Central Tibet: Products of lithospheric delamination beneath the Lhasa–Qiangtang collision zone. Lithos 198, 24–37.
Wang, B.D., Wang, L.Q., Chung, S.L., Chen, J.L., Yin, F.G., Liu, H., Li, X.B., Chen, L.K., 2016. Evolution of the Bangong–Nujiang Tethyan Ocean: insights from the geochronology and geochemistry of mafic rocks within ophiolites. Lithos 245, 18–33.
Wang, X.S., Williams-Jones, A., Bi, X.W., Hu, R.Z., Xiao, J.F., Huang, M.L., 2019. Late cretaceous Transtension in the Eastern Tibetan Plateau: evidence from Postcollisional A-Type Granite and Syenite in the Changdu Area, China. J. Geophys. Res. Solid Earth 124, 6409–6427.
Workman, R.K., Hart, S.R., 2005. Major and trace element composition of the depleted MORB mantle (DMM). Earth Planet. Sci. Lett. 231, 53–72.
Wu, F.Y., Jahn, B.M., Wilde, S.A., Lo, C.H., Yui, T.F., Lin, Q., Ge, W.C., Sun, D.Y., 2003. Highly fractionated I-type granites in NE China (I): geochronology and petrogenesis. Lithos 66, 241–273.
Wu, R.X., Zheng, Y.F., Wu, Y.B., Zhao, Z.F., Zhang, S.B., Liu, X., Wu, F.Y., 2006. Reworking of juvenile crust: element and isotope evidence from Neoproterozoic granodiorite in South China. Precambrian Res. 146, 179–212.
Wu, F.Y., Liu, X.C., Ji, W.Q., Wang, J.M., Yang, L., 2017. Highly fractionated granites: Recognition and research. Sci. China Earth Sci. 60, 1201–1219.
Wyllie, P.J., 1977. Crustal anatexis: an experimental review. Tectonophysics 43, 41–71.
Yi, J.K., Wang, Q., Zhu, D.C., Li, S.M., Liu, S.A., Wang, R., Zhang, L.L., Zhao, Z.D., 2018. Westward-younging high-Mg adakitic magmatism in Central Tibet: Record of a westward-migrating lithospheric foundering beneath the Lhasa–Qiangtang collision zone during the late cretaceous. Lithos 316, 92–103.
Yu, H.X., Chen, J.L., Xu, J.F., Wang, B.D., Wu, J.B., Liang, H.Y., 2011. Geochemistry and origin of late cretaceous (similar to 90Ma) ore-bearing porphyry of Balazha in mid-northern Lhasa terrane, Tibet. Acta Petrol. Sin. 27, 2011–2022 (in Chinese with English abstract).
Zhang, Z.M., Zhao, G.C., Santosh, M., Wang, J.L., Dong, X., Shen, K., 2010. Late cretaceous charnockite with adakitic affinities from the Gangdese batholith, southeastern Tibet: evidence for Neo-Tethyan mid-ocean ridge subduction? Gondwana Res. 17, 615–631.
Zhang, K.J., Zhang, Y.X., Tang, X.C., Xia, B., 2012. Late Mesozoic tectonic evolution and growth of the Tibetan plateau prior to the Indo–Asian collision. Earth Sci. Rev. 114, 236–249.
Zhang, K.J., Xia, B., Zhang, Y.X., Liu, W.L., Zeng, L., Li, J.F., Xu, L.F., 2014. Central Tibetan Meso-Tethyan oceanic plateau. Lithos 210, 278–288.
Zhao, T.P., Zhou, M.F., Zhao, J.H., Zhang, K.J., Chen, W., 2008. Geochronology and geochemistry of the c. 80 Ma Rutog granitic pluton, northwestern Tibet: implications for the tectonic evolution of the Lhasa Terrane. Geol. Mag. 145, 845–857.
Zheng, Y.F., Zhang, S.B., Zhao, Z.F., Wu, Y.B., Li, X., Li, Z., Wu, F.Y., 2007. Contrasting zircon Hf and O isotopes in the two episodes of Neoproterozoic granitoids in South China: implications for growth and reworking of continental crust. Lithos 96, 127–150.
Zhu, D.C., Pan, G.T., Mo, X.X., Wang, L.Q., Zhao, Z.D., Liao, Z.L., Geng, Q.R., Dong, G.C., 2006. Identification for the Mesozoic OIB-type basalts in central Qinghai–Tibetan Plateau: Geochronology, geochemistry and their tectonic setting. Acta Geol. Sin. 80, 1312–1328 (In Chinese with English abstract).
Zhu, D.C., Zhao, Z.D., Niu, Y.L., Dilek, Y., Hou, Z.Q., Mo, X.X., 2013. The origin and pre-Cenozoic evolution of the Tibetan Plateau. Gondwana Res. 23, 1429–1454.
Zhu, D.C., Li, S.M., Cawood, P.A., Wang, Q., Zhao, Z.D., Liu, S.A., Wang, L.Q., 2016. Assembly of the Lhasa and Qiangtang terranes in Central Tibet by divergent double subduction. Lithos 245, 7–17.
Zhu, D.C., Wang, Q., Chung, S.L., Cawood, P.A., Zhao, Z.D., 2018. Gangdese Magmatism in Southern Tibet and India–Asia Convergence since 120 Ma. Geological Society London Special Publications.